Comparison of two- and three-dimensional full waveform inversion imaging using wide-angle seismic data from the Deep Galicia Margin

Bhargav Boddupalli[1*], Tim A. Minshull[1], Joanna Morgan[2], Gaye Bayrakci[3] and Dirk Klaeschen[4]

[1]School of Ocean and Earth Science, University of Southampton, SO14 3ZH, UK.

[2]Department of Earth Sciences and Engineering, Imperial College London, SW7 2AZ, UK.

[3]National Oceanography Centre Southampton, SO14 3ZH, UK.

[4]GEOMAR, Helmholtz Centre for Ocean Research Kiel, 24148, Germany.

[*]now at Institute for Geophysics, University of Texas at Austin, USA

Corresponding author: Bhargav Boddupalli

Email address: bhargav@ig.utexas.edu

In original form date: 07th August 2020

SUMMARY

Full waveform inversion (FWI) is a data-fitting technique capable of generating high-resolution velocity models with a resolution down to half the seismic wavelength. FWI is applied typically to densely sampled seismic data. In this study, we applied FWI to 3D wide-angle seismic data acquired using sparsely spaced ocean bottom seismometers (OBSs) from the Deep Galicia Margin west of Iberia. Our dataset samples the S-reflector, a low-angle detachment present in this area. Here we highlight differences between 2D, 2.5D and 3D-FWI performances using a real sparsely spaced dataset. We performed 3D FWI in the time domain and compared the results with 2D and 2.5D FWI results from a profile through the 3D model. When overlaid on multichannel seismic images, the 3D FWI results constrain better the complex faulting within the pre- and syn-rift sediments and crystalline crust compared to the 2D result. Furthermore, we estimate variable serpentinisation of the upper mantle below the S-reflector along the profile using 3D FWI, reaching a maximum of 45%. Differences in the data residuals of the 2D, 2.5D and 3D inversions suggest that 2D inversion can be prone to overfitting when using a sparse dataset. To validate our results, we performed tests to recover the anomalies introduced by the inversions in the final models using synthetic datasets. Based on our comparison of the velocity models, we conclude that the use of 3D data can partially mitigate the problem of receiver sparsity in FWI.

Keywords: Waveform inversion, Controlled source seismology, crustal imaging

1. Introduction

Seismic imaging is one of the most widely used tools for understanding crustal processes. Advances in seismic imaging are mainly driven by the hydrocarbon exploration industry. In academia, first arrival travel-time tomography (FATT) using long-offset refraction data is a widely used method to obtain smooth velocity models of the crust (e.g. Hammer et al. 1994; Zelt & Barton 1998). A drawback of the FATT method is its resolution, which is limited at best

to the width of the first Fresnel zone. In addition, the presence of low-velocity zones can pose difficulties for identifying the first arrivals in the data. To deal with such problems, seismic imaging studies are moving forward towards higher-resolution techniques like waveform inversion, which utilise more information in the waveform record to derive finer resolution models. The full waveform inversion (FWI) technique was proposed by Lailly (1983) and Tarantola (1984) as a linearized inverse problem using adjoint operators. Advances in computational facilities and seismic data acquisition techniques have greatly supported the development of FWI. FWI is capable of resolving structures to half the shortest seismic wavelength present in the data. Moreover, it accounts for information beyond the traveltimes of the waveform depending upon the wave attributes inverted during the inversion. However, higher resolution comes at a cost of large computational requirement and increased non-linearity of the inverse problem. Obtaining the correct solution using FWI largely depends on how well-posed is the inverse problem.

Wide-angle seismic data are well suited for performing FWI because they are rich in low-frequencies. Furthermore, OBSs enable recording of long-offset marine seismic data given a powerful source, which otherwise is not possible using a limited-offset streamer. Although wide-angle acquisition using OBSs has been widely conducted in last few decades, FWI techniques have rarely been applied to these data until recently. In academia, the main concern in using a wide-angle dataset for FWI is the data sparsity. A sparse dataset may cause the inversion to fail to converge to the right solution due to a poorly constrained inverse problem. The first application of FWI to synthetic wide-angle data was demonstrated by Pratt et al. (1996) in 2D in the frequency domain, while real data applications were demonstrated by Dessa et al. (2004) and Operto et al. (2006). In the last few years, different variants of FWI have been applied to OBS data from different tectonic settings, restricted mostly to 2D (e.g., Górszczyk et al. 2017, 2019; Kamei et al. 2013). Morgan et al. (2016) demonstrated the application of 3D

71 acoustic, anisotropic FWI to a sparse dataset from the Juan de Fuca Ridge, revealing low-
72 velocity zones interpreted as magmatic-hydrothermal reaction zones. Using a similar approach,
73 Davy et al. (2018) presented isotropic high-resolution models using sparsely spaced and noisy
74 2D OBS data from the Deep Galicia margin west of Iberia. The dataset used by Davy et al.
75 (2018) is a subset of the 3D dataset used in this study.
76 The Galicia margin has been a testing ground for various hypotheses on rifting, that explain
77 the observed crustal thinning, reduced mantle velocities, and mantle exhumation (e.g., Boillot
78 et al. 1987; Reston 2009). This margin is a sediment starved and magma-poor margin allowing
79 optimal resolution of features using geophysical imaging. Seismic studies in this region have
80 revealed many interesting observations over last few decades (e.g., Boillot et al. 1980;
81 Whitmarsh et al. 2001). 3D seismic reflection imaging has enabled unique insights into the
82 rifting tectonics in the margin, including 3D interpretation of the fault structures, identification
83 of the coherent corrugations on the S-surface and identification of the S-interval (Lymer et al.
84 2019; Schuba et al. 2018). 2D and 3D tomographic models derived using wide-angle seismic
85 data were used to identify thin oceanic crust west of the margin and estimate serpentinisation
86 below the S-reflector (Bayrakci et al. 2016; Davy et al. 2016)
87 In this paper, we performed 3D FWI using wide-angle seismic data recorded by 40 OBSs in
88 the Deep Galicia Margin (DGM) assuming an acoustic and isotropic medium. We also
89 performed 2.5D and 2D FWI using subsets of the dataset and compared the 3D FWI result with
90 2D and 2.5D FWI results. 3D wide-angle data have the potential to improve the resolution of
91 subsurface velocity structure compared to 2D because of the extra data recorded from the shot
92 lines away from the receivers, but 2D wide-angle studies are more common than 3D studies.
93 Hence, we aim to highlight differences in imaging between 2D, 2.5D and 3D approaches using
94 a real sparse dataset, and illustrate the limitations in resolution of 2D and 2.5D FWI imaging

in a rifted margin setting compared to 3D. A detailed interpretation of full 3D FWI results will be presented elsewhere.

2. Geological Setting

The West Iberia margin is a magma-poor rifted margin where rifting is thought to have occurred in several phases (e.g. Murillas et al. 1990; Péron-Pinvidic et al. 2007; Tucholke et al. 2007). In the early stages of rifting during the late Triassic to early Jurassic, the fault-bounded Lusitanian and Galicia Interior Basins were formed (Figure 1; Murillas et al. 1990; Tucholke et al. 2007). During the Late Jurassic to Early Cretaceous, the Galicia Interior Basin developed further westward on the Galicia margin, thinning the continental crust to 15 km (Pérez-Gussinyé et al. 2003). In the final stages, the extension was primarily focused in the DGM, thinning the crust to less than 5 km (Murillas et al. 1990) and exhuming the subcontinental mantle lithosphere (Boillot & Winterer 1988; Tucholke et al. 2007). The DGM is a hyperextended zone characterised by west-dipping normal faults that sole into a detachment fault (Figure 1; Reston et al. 1996, 2007). Here, the continental crust comprises tilted fault blocks of crystalline basement rocks overlain by pre-, syn- and post-rift sediments. Various mechanisms are proposed to explain the faulting pattern, crustal thinning, asymmetry on the conjugate margins and role of the detachment fault in continental break-up. The detachment fault underlying the fault blocks is called the S-reflector, which is imaged as a bright reflector on seismic sections in this region (De Charpal et al. 1978; Lymer et al. 2019; Reston et al. 1996, 2007; Schuba et al. 2018). It is interpreted as a boundary separating the continental crust above from the serpentinised mantle below (Leythaeuser et al. 2005; Reston et al. 1996). Westward of the thinned continental crust lies a narrow, north-south oriented ridge with 2-4 km of relief. Based on direct sampling, this ridge is interpreted as exhumed mantle and is known as the Peridotite Ridge (e.g. Beslier et al. 1993; Boillot et al. 1980). Similar ridges are identified along-strike on the West Iberia margin (Beslier et al. 1993). At the DGM, exhumed

mantle is postulated to extend seaward by at least 85 km from the Peridotite Ridge (Davy et al. 2016; Dean et al. 2015). Under the influence of continuous stretching during rifting, the entire crust was thinned to less than 10 km, inferred to have made it cooler and brittle and to have coupled the lower and upper crust (Pérez-Gussinyé et al. 2003; Pérez-Gussinyé & Reston 2001). The normal faults cut through the entire crust, acting as fluid conduits, transporting seawater to the upper mantle and serpentinising the upper mantle peridotites (Bayrakci et al. 2016; Pérez-Gussinyé & Reston 2001; Reston 2007). Using P-wave velocities derived from wide-angle seismic data, Bayrakci et al. (2016) and Davy et al. (2018) presented the evidence for preferential hydration of the upper mantle close to the normal faults, with maximum serpentinisation of 45%.

3. Seismic data

The Galicia-3D (G3D) experiment was conducted at the DGM from June to August 2013, to acquire a multichannel reflection and coincident wide-angle seismic data. Wide-angle data were recorded within the 3D box using 78 ocean bottom hydrophones/seismometers (Figure 2). The *FS Poseidon* deployed and recovered the OBSs, which concurrently recorded the signals from the seismic reflection experiment. OBSs were deployed in four lines with a spacing of ~6.5 km between the lines (Figure 2). The mean spacing between OBSs along each line is ~3.2 km. In this study, wide-angle data recorded by the hydrophones were used because of the absence of geophones on some instruments. The multichannel reflection seismic volume, acquired by the *RV Marcus G. Langseth*, was processed over an area of 68.5 km (east-west) by 20 km (north-south) (Figure 2). The 3D seismic reflection data were acquired using four 6 km streamers towed 200 m apart. The survey was carried out using two air-gun arrays each consisting of 20 airguns. The two arrays were towed 100 m apart with gun volumes between 40 cu.in. and 360 cu.in. at a depth of 9 m. The total individual volume of each airgun array was 3,300 cu.in.. Seismic shots were fired alternately using two source arrays every 37.5 m (shot

145 interval of ~ 16 s with ship speed of 4.5 knots). Processing of the reflection seismic data set
146 was performed by Repsol, who produced a 3-D pre-stack Kirchhoff time migrated seismic
147 volume.
148

149 **4. Full-waveform inversion**

150 FWI technique involves iteratively updating a starting model using a least-squares local
151 inversion and the Born approximation (Lailly 1983; Tarantola 1984). The basic equation that
152 is solved in the FWI is:

$$\bar{m} = G^{-1} d_o \quad (1)$$

153 where d_o is the observed data; G^{-1} is the inverse of the forward modelling operator (G); and
154 $\bar{m}$ is the inverted model. There is no formal method to estimate G^{-1} from G. Hence, the solution
155 to the inverse problem is achieved with an iterative approach using gradient based methods. In
156 this study, we perform 3D FWI in the time domain using the FULLWAVE code (Warner et al.
157 2013). The starting model is updated in steps by reducing the residuals between the observed
158 and predicted data generated with a forward modelling algorithm, which in our case uses the
159 finite difference method (Warner et al. 2013). The root-mean square (RMS) amplitude of the
160 predicted dataset is scaled to match the RMS of the observed data trace-by-trace, and a broad
161 sliding time-window is applied during the modelling so that different phases are normalised
162 independently (Warner et al. 2013). The misfit (*f*) between predicted and observed datasets is
163 calculated by summing the squares of the differences between the trace-by-trace normalised
164 predicted (d_p) and observed (d_o) data, for every time sample:

$$\boldsymbol{f} = \frac{\mathbf{1}}{\mathbf{2}} \left\| \frac{\boldsymbol{d_p}}{\|\boldsymbol{d_p}\|_2} - \frac{\boldsymbol{d_o}}{\|\boldsymbol{d_o}\|_2} \right\|_2^2 \quad (2)$$

Assuming a linear relationship between model perturbation and data residual, the model update is given as

$$\boldsymbol{\delta m = -H^{-1}\frac{\partial f}{\partial m}} \quad (3)$$

where H is the Hessian matrix containing all the second-order differentials of the functional f with respect to model parameters, and $\frac{\partial f}{\partial m}$ is the gradient of the functional with respect to each of the model parameters. The gradient term is computed by taking a zero-lag cross-correlation between the source generated forward-propagated wavefield and residual generated back propagated wavefield using the adjoint source (Tarantola 1984). The computation of the Hessian matrix is avoided by replacing the Hessian with a scaling parameter using the steepest-descent algorithm for optimisation. Density is estimated from the velocities using Gardner's law below the seafloor and is fixed during the inversion step (Gardner et al. 1974).

4.1 FWI Workflow

We followed the workflows of Warner et al. (2013) and Morgan et al. (2016):

1. Generating the source wavelet
2. Determining the starting model
3. Determining the starting frequency
4. Pre-processing the data
5. Defining the modelling and inversion strategy
6. Quality assurance

4.1.1 Generating the source wavelet

The source wavelet was generated by developing a Wiener filter. Building the wavelet involved the following steps: 1) extracting the nearest offset (<50 m) direct water-wave arrivals from a few selected OBSs, muting the arrivals after 1 second to minimise contamination by subsurface properties; 2) aligning the direct water-wave on every individual trace to the same time (say

3.5 seconds); 3) stacking the traces to obtain a mean trace for the direct-water wave at one OBS location and resampling the trace to 1 ms; 4) generating a synthetic trace using a random guess wavelet and water column velocities for the same selected OBS (the guess wavelet should be band-pass filtered in the same way as the data and resampled to 1 ms); 5) repeating steps 1 and 2 for the synthetic trace by extracting and adjusting the direct water arrival time; 6) matching the synthetic trace with the observed trace to obtain an inverse filter using the Wiener method; 7) convolving the inverse filter with the guess wavelet to build the source wavelet; and 8) verifying the source wavelet by re-generating synthetic data and comparing it with the observed OBS data.

4.1.2 Starting model

The starting velocity model is an important component of FWI. To qualify as a starting model for FWI, a velocity model should be able to predict the observed data within half a wavelength at the starting frequency. The starting model used for FWI in this study was derived from FATT of the wide-angle seismic data recorded by OBSs from Galicia3D experiment presented by Bayrakci et al. (2016). The authors used the First Arrival Seismic Tomography code, which solves the Eikonal equation using finite difference scheme and optimization using the LSQR variant of the conjugate gradient algorithm (Paige & Saunders 1982; Zelt & Barton 1998). The RMS misfit for the final FATT model is 73 ms and the chi-squared value is 1. We modify this model by replacing a constant water velocity of 1520 m/s with the water column velocity profile measured during data acquisition to improve the accuracy of the first arrival predictions in the forward modelling, and linearly interpolating the grid from 500 m spacing to 50 m, to ensure an accurate and smooth seafloor. Although the final inversion runs were performed using a 50 m grid spacing, most of the test runs initially were performed using a grid spacing of 100 m to reduce computational time. A 3D linear interpolation technique was used to interpolate the model from 500 m to 100 m and then further to 50 m after application of

213 smoothing filters described below. Cubic-spline, near-neighbour and linear interpolation
214 techniques were all tested. The spline method introduced spurious values at the seafloor around
215 the edges of the Peridotite Ridge, and the near-neighbour technique resulted in a pixelated
216 model as it uses just the neighbouring points for calculating values at intermediate grid points.
217 Use of a linear interpolation technique overcame these shortcomings and resulted in a smoother
218 starting model compared to the near-neighbour technique. Smooth starting models without
219 sharp velocity contrasts are preferred for FWI, unless such contrasts are well-constrained, such
220 as the seafloor (Morgan et al. 2016). Therefore a further smoothing process was carried out
221 using a 2D convolutional filter applied along each profile of the 3D velocity model. Prior to
222 the application of the filter, the velocity model was converted into a slowness model and
223 vertically resampled to 1 m. The filter was applied over a window with dimensions 200 m
224 vertically and 1500 m horizontally to remove any sharp velocity changes.
225 The adequacy of the starting model was tested for its ability to predict the data within half a
226 seismic wavelength for all instruments. The phase plots, plotting the phases of the first arrivals,
227 assured the adequacy of the starting model by indicating that the starting model is not cycle-
228 skipped (Figure 3). The phases are computed by applying a Fourier transform to each
229 windowed trace to include just the first arrival and extracting the phase at a particular frequency
230 (Warner et al. 2013). The concentric nature around the OBS of the phase changes of the first
231 arrival with increasing offset indicates a good signal-to-noise ratio to maximum offset of ~15
232 km. At ~15 km offset, the phase plots for the observed data show more chaotic behaviour
233 indicating poor signal to noise ratio (Figure 3a and b). If the starting model, compared to the
234 observed data, is not cycle-skipped, then the phase change is smooth and consistent with offset
235 whereas if it is cycle-skipped there will be sudden jumps in the phase (Shah et al. 2012). The
236 phase residuals were calculated by subtracting phases of the first arrivals of the observed data
237 from the synthetic data. The phase of the first arrivals of the predicted and observed data were

compared to check if the predicted data were within an acceptable limit ($-\pi$ to $+\pi$) (Figure 3e and f). Further verification was carried out by plotting sets of 10 traces from each dataset – observed and predicted – alternating to manually check for poor fit (Figure 4).

4.1.3 Starting frequency

Non-linearity of the inverse problem can be partially mitigated by starting the inversion from the lowest frequency available in the data and progressing towards higher frequencies (Bunks et al., 1995). The choice of the starting frequency for our inversion is based on examining the phase of the first arrivals in the observed data with increasing offset (Figure 3a and b). The RMS values of the phase residuals at 2.7 and 3 Hz are 1.42 and 1.44 radians, respectively. RMS values well below π radians clearly indicate that the starting model is able to predict the phase of the first arrivals within the acceptable limits, and the starting frequency for the inversion can be 2.7 or 3 Hz. Test inversion results performed using a subset of the dataset starting from 2.7 Hz and 3 Hz did not show significant differences. The RMS amplitude of the difference between the results of these test runs is equal to 36 m/s with the largest perturbation value equal to 236 m/s (Figure 5). Hence, we started the final inversion run by applying low-pass filter rolling off at 3 Hz to reduce the computational time, rather than following the fundamental notion of starting the inversion from the lowest possible frequency (Sirgue, 2006).

4.1.4 Pre-process the data

A minimum-phase Ormsby bandpass filter with corner frequencies of 2-3 to 5-7 Hz was applied to reduce the random noise in the input data. The limits for the band-pass filter were chosen after trying different frequency ranges. The same filter was also applied to the source wavelet. Manually picked mute gates were applied to each OBS to include only the first arrivals. The unmuted window lengths were customized depending on the match of the observed traces with the synthetic traces generated using the starting model (Figure 4). The window lengths varied between 700 ms and 1200 ms for all the instruments. Data up to maximum offset of 15 km

were included into the inversion, beyond which the data quality was degraded by arrivals from the previous shot, making it unsuitable for FWI.

4.1.5 Modelling strategy

We inverted only for P-wave velocities, assuming isotropic and acoustic approximations for the medium. These assumptions are based on the previous tomographic and FWI studies in this region using the same wide-angle dataset, which indicated an absence of strong elastic and anisotropic effects (Bayrakci et al. 2016; Davy et al. 2018). In this work, we developed a 2D velocity model using only two nearby shot lines from the instruments along line 2, a 2.5D velocity model using all shots from the instruments along line 2, and a 3D velocity model using wide-angle data from OBSs along lines 1, 2 and 3 (Figure 2).

Wide-angle refraction data from 40 OBSs were considered for the 3D inversion (Figure 2). The number of profiles recorded by each instrument was 100. Data from the northernmost line (line 4) of OBSs were not included because of larger uncertainty in their re-located positions, which is partly due to the lack of a shooting profile directly above the OBSs. Profiles with low signal-to-noise ratio on a particular OBS were excluded from the inversion. Only data that were predicted by the starting model within a half seismic wavelength were included in the 2.5D and 3D inversions (Appendix A). Data from OBS 51 were not included in the 2D FWI because the data along the closest shot lines were not recorded by this instrument, but were included in the 2.5D and 3D FWI. Data from OBSs 80 and 85 were not used in our inversions because the starting model was unable to predict the data accurately due to time shifts that we were unable to correct.

The maximum and minimum velocities in the starting model are 1497 and 8000 m/s, respectively. The grid spacing in the velocity model is 50 m in each of the three dimensions. To ensure that the wavefield is computed in at least two locations in every cell given the maximum velocity in the starting model, the sampling interval of the input data should be less

than 3.125 ms (0.5 * grid spacing/maximum velocity; Lines et al., 1999). Hence, the data were resampled to 3 ms to satisfy this condition. The grid dimensions in the inline and crossline directions were chosen to include all the receivers and shots within the grid and to avoid edge effects in the wave propagation, which requires shots falling within 1 km of the edge of the grid to be removed. The dimensions of the grid along the inline (along the shooting profiles) and crossline (across the shooting profiles) directions are 78.5 km and 22.1 km, respectively, and the vertical dimension is 12 km. To facilitate the implementation of the code, a data reciprocity rule was applied to treat the shots as receivers and OBSs as shots. The inversion was performed following the multi-scale approach starting from low frequencies and progressing towards higher frequencies in steps (Bunks et al. 1995). During the inversion, the program applies low-pass filters, in steps rolling off at frequencies 3, 3.3, 3.9, 4.5 and 5.2 Hz, to the data and the source wavelet (Warner et al. 2013). Thirty iterations were performed at each filter setting to allow the misfit functional to reduce and flatten. For the final inversion run, smoothing was applied to the gradient using a Gaussian filter with correlation lengths of 2 x seismic wavelength and 1 x seismic wavelength in the horizontal and vertical directions, respectively. The seismic wavelength for gradient smoothing was calculated using the local velocity in the model and the rolling off frequency specified for the current iteration. These smoothing parameters were adjusted to suppress short-wavelength artefacts in the result. 2.5D and 2D inversions were performed using same parameterisation as 3D inversion but included data only from instruments along line 2. The total number of shots for the 3D, 2.5D and 2D inversions are 84768, 55591 and 1792, respectively. For the 2D inversion, two shot lines were used from 16 OBSs along line 2 (Figure 2) and projected onto an imaging line closest to line 2. The velocity model dimensions for the 2D inversion were 78.5 km in the horizontal direction and 12 km in the vertical dimension.

FWI is a computationally demanding imaging technique, so forward modelling and inversion runs were performed on two large linux clusters: Iridis 5 (University of Southampton) and Mobilis (National Oceanography Centre). Mobilis comprises 72 computing nodes each with 64 GB of memory (DDR3 memory) and 2 x Intel Xeon E5-2650 2.6 GHz eight-core processors, giving a total of 1152 processor cores. Iridis 5 comprises of 464 compute nodes with dual 2.0 GHz Intel Skylake processors. Each compute node has 40 CPUs per node with 192 GB of DDR4 memory. Initial testing and 2D inversions were performed on Mobilis because of its smaller queue time, whereas the final 3D inversion runs were performed on Iridis 5. The 2D inversion run was performed by assigning 4 OBSs to each node, while for 3D inversion 2 OBSs were assigned to each node. In 3D inversions, no extra CPUs/nodes were assigned for the OBSs that have just two shot lines recorded (Figure 2). Runs on Mobilis were performed using 4 nodes and the computation time for each iteration was ~1 minute in the final 2D inversion run. For the final 3D inversion run, 18 nodes were employed on Iridis 5, with one extra node reserved for communication between the nodes. The compute time for each iteration for the 3D run was ~45 minutes.

4.1.6 Quality assurance

We tracked the progress of the 3D inversion by monitoring the phase residuals, obtained by subtracting the phases of the predicted and observed data (Figure 6). These phase residuals clearly have reduced after the first iteration at both frequencies (Figure 6c and d). Abrupt changes from one extreme phase to other ($-\pi$ to $+\pi$) indicate cycle-skipping, which is not observed except for a few noisy traces at the far and near offsets. Including a substantial number of cycle-skipped traces into the inversion could cause it to converge to a local minimum that is not the global minimum. However, if the number of such traces is small, the effects from cycle-skipped traces are nullified by the rest of the data driving the model towards the global minimum (Shah et al. 2012). For most of the data the phase change is gradual at 3 Hz, except

for a very few traces at far offsets that have poorer signal-to-noise ratio (Figure 6). At 4.5 Hz, there are regions that change their phases abruptly from red to blue. However, these same regions show small phase changes at 3Hz. There is a gradual improvement as the inversion progresses without cycle-skipping, and the phase difference for most of the traces is close to zero for the final model (Figure 6e and f). This is a clear advantage of progressing from lower frequencies to higher frequencies during the inversion. At lower frequencies, the probability of cycle-skipping is lower because the misfit function near the global minimum is smoother and broader, hence reducing the chance of getting trapped in a local minima. To further check the convergence of the FWI, we plotted the predicted data from the travel-time model and FWI inverted model with the observed data to check the improvements resulted from FWI (Figure 7; Appendix B). The result shows clear improvement in the alignment of the FWI model synthetics with the observed data compared to the travel-time model synthetics.

5. Results and discussion

We compare the results from 2D, 2.5D and 3D FWI along the seismic line 420 (OBS line 2) in both depth and time domains (Figure 2, 8 and 9). In our comparison, we have also included the 2D FWI result from Davy et al. (2018), which was derived along the same line using the wide-angle data from the OBSs, but from a different starting model (from Davy et al. 2016). Our 2D result is derived using just two shot profiles closest to the instruments along line 2 and the starting velocity model was obtained from the 3D travel-time model by extracting a profile closest to the shots and instruments along line 2 (Bayrakci et al. 2016). In order to highlight the differences between 2D, 2.5D and 3D imaging, we overlaid the time-converted velocity profiles on a time-migrated seismic section obtained from 3D seismic volume (Figure 9; Lymer et al. 2019). The interpretations used in our comparison were developed through the entire 3D reflection seismic volume and are independent of our FWI velocity models (Lymer et al. 2019). In the text that follows, we use the following abbreviations: 2DA corresponds to 2D FWI result

of Davy et al. (2018), 2DB corresponds to our 2D FWI result with shots and receivers projected onto an imaging line, 2DC corresponds to the 2D FWI result with shots and receivers at their actual locations, 3DA corresponds to the 2.5D inversion using data from instruments along line 2 and 3DB correspond to full 3D results.

5.1 2D FWI

5.2.1 2DA vs 2DB:

The inversion strategy of the 2DA FWI result differs from that of the 2DB FWI result in the length of the average unmuted time window applied to the input seismic data, the maximum offset of data used for the inversion and the smoothing parameters applied to the models during the inversions. These differences are likely to be the primary reason for the differences observed in the two sections, especially the short wavelength structures (Figures 8a-b and 9a-b). In addition, the starting models used for 2DA and 2DB are derived from different studies (Figures 8a-b, 9a-b; Bayrakci et al. 2016; Davy et al. 2016). In 2DA, the starting model was derived from 2D travel-time tomography, in which the thickness of the sediment column is also constrained using the top basement depths from the multichannel images. Such a modelling approach resulted in improved fit of the top of the basement with the multichannel images, which is evident at the Peridotite Ridge compared to the result from 2DB (Figure 8). In both the results, the long wavelength structure fits the interpreted top of the pre- and syn-rift sediments and crystalline crust well, indicating that different starting models generated a similar background model. However, the finer details within the fault blocks and the undulations at the S-reflector differ between the images.

5.2.2 2DB vs 2DC:

Traditionally in 2D imaging the shots and receivers locations are projected onto an imaging line, which results in errors in wave propagation. However, if the projections are within an acceptable distance from their actual locations to the closest imaging line passing through the

388 shots and receivers, the resulting errors would be insignificant. Performing synthetic tests with
389 the projected locations can validate these approximations, in which anomalies introduced
390 artificially into the velocity model are recovered using synthetic data. Such a synthetic test was
391 performed for the 2DB case, and the introduced anomalies were recovered during the inversion
392 using the same starting model used for 2DB inversion (Figure 14a-b; Bayrakci et al. 2016).
393 The result from this test is discussed in detail in the section 6. Although the synthetic test
394 validated the approximations considered in the 2DB case, we performed another 2D inversion
395 (2DC) using the actual shot and receiver locations to highlight the differences in 2D imaging
396 due to the projected locations. In order to consider their actual locations, we performed the
397 2DC inversion using a narrow 3D velocity grid of width 2 km in the crossline direction
398 encompassing the shots and receivers along the line 2 (Figure 2). The other dimensions of the
399 velocity grid were the same as the 2DB case and the starting model was extracted from the 3D
400 travel-time tomography (Bayrakci et al. 2016). Also, the number of shots and receivers used in
401 2DC were the same as the 2DB case. The models 2DB and 2DC compare well up to a depth of
402 8 km and show large differences in the deeper regions of the model (Figure 10). At the S-
403 reflector, 2DB shows velocities greater than 6.5 km/s, whereas the velocities in 2DC are less
404 than 6.5 km/s (Figure 10). In principle, these two inversion runs should generate similar
405 images, considering that the errors from shots and receiver locations are insignificant.
406 However, predominantly large differences below 8 km depth suggest that the 2D imaging has
407 resulted in a non-unique model of the deeper sections (Figure 10). It is arguable that the 2DC
408 inversion results in more accurate 3D amplitudes than the 2DB inversion, therefore giving rise
409 to the difference in the images. Seismic data generated using 3D and 2D codes produce
410 synthetic data with a factor of $\sqrt{t}$ difference in amplitudes (where t is travel-time). Since the
411 2DC inversion uses a narrow 3D grid the amplitudes of the synthetic arrivals will better match
412 the observed, and this may lead to differences in the 2DC and 2DB images. However, in the

FWI code used here, the input data are normalised using a broad sliding window, and this has a net effect of minimising the effect of amplitude differences due to a 2D approximation, attenuation, elasticity etc (Warner et al. 2013).

Although 2D FWI results show a reasonable match with the multichannel seismic image (Figure 8a-b, 9a-b), differences in the short-wavelength structures are noticeable. Compared to the 3D starting model, all the 2D results show an improved fit to the multichannel images especially along the top basement blocks (Figure 9). Our preferred 2D FWI model for this study is 2DB because it has been developed following the conventional 2D procedure by projecting shots and receivers unto the imaging line. Also, the parameters used in developing 2DB are the same as the 3D inversions making it more suitable for comparison.

5.2 3D FWI

Both 3D velocity models have resolved the structures that are geologically relevant, but there are differences between them (Figure 8). To highlight the differences between 3D models, we carried out a detailed comparison of the images based on the match between the velocity models and multichannel seismic images, focusing on the pre- and syn-rift sediments, the basement blocks and the S reflector. We also include the 2D FWI models in the following discussion.

5.2.1 Pre- and syn-rift sediments:

Pre- and syn-rift sediments are interpreted by Lymer et al. (2019) between the boundaries of the base of the post-rift sediments (dashed blue line) and top of the crystalline crust (dashed red line) (Figures 8 and 9). All of the 2D and 3D FWI results resolve the long wavelength structure in this zone well, as indicated by their match with the multichannel interpretations. The velocities of pre- and syn- rift sedimentary packages range from ~3.5 km/s to ~5.25 km/s overlying the crystalline crust along this profile. The 3.5 km/s velocity contour tends to oscillate in the FWI results compared to the starting model, and the pattern of the oscillations

is inconsistent between different 2D and 3D results beyond 25 km (Figure 8 and 9). This oscillatory pattern is likely to be the result of complex faulting within the pre- and syn-rift packages which has been previously interpreted in multichannel seismic images from the Deep Galicia margin (Lymer et al. 2019; Ranero & Pérez-Gussinyé 2010; Reston 2005). Such a fine-scale faulting pattern is beyond the resolution limits of our inversions, primarily because of the absence of high-frequency content in our dataset. However, the oscillations are smaller in the 3DB result than in the 3DA and all 2D results. Although the contour shows short-wavelength perturbations (oscillations) within the pre- and syn-rift sediments, it shows an improved alignment with the faults compared to the starting model, especially along faults F5, F4 and F3 (Figure 9).

Our 3DA model shows artefacts within the sedimentary column, which are vertical in nature and lie beneath the OBS positions (Figure 8 and 9). These artefacts are mainly observed in the western region of the model between the Peridotite Ridge and the crustal blocks. They arise from the inclusion of shot profiles away from the OBS locations. Arrivals from the far-offset profiles travel through deeper parts of the model that are not well constrained in the 3DA inversion, because in 3DA there are no other OBSs located between the far-offset shot profiles and the OBS location to constrain deeper parts of the model. Further, the fact that these artefacts are not observed in the 2DB and 3DB models supports the above explanation. Another contributing factor for these artefacts may be the high uncertainty of the starting model in the western part (Bayrakci et al. 2016).

5.2.2 Crystalline crust:

For all the FWI models, the crystalline crustal section shows a significantly better match than the starting model to the multichannel seismic image (Figure 9). The velocity range for crystalline basement inferred from our results is ~5.25 km/s to ~6.5 km/s. All of the 2D models show circular velocity contours in some locations within the crust, which are geologically

unrealistic. Such structures can be a result of a poorly constrained inverse problem or from the assumed approximation of the wave equation as acoustic, isotropic and non-attenuating. However, these circular features would also be observed in 3D imaging if the assumed approximations of the wave equation do not apply to the real Earth model in the study region. A good match of the 3DB velocities within the crystalline crust with multichannel images supports the 3D nature of crustal fault-blocks.

5.2.3 S-reflector and serpentinisation:

Previously, the 3D travel-time model has shown that velocity 6.5 km/s contour follows well the S-reflector (Bayrakci et al. 2016). However, FWI results have introduced undulations in the 6.5 km/s contour in both 2D and 3D. 2DA and 2DB show different velocity patterns at S that are highlighted by the 6.5 km/s contour. The reason for this difference may be the different inversion strategies for the two cases, particularly the choice of the window lengths, smoothing parameters and offsets for the input data. Although the 2DA and 2DB models predict higher velocities than 6.5 km/s at S compared to the starting model, it is observed that 2D imaging has generated non-unique models at S in the section 5.1. To explore the velocities below the S-reflector, we plotted average velocity values below the S-reflector over a window of 100 ms along line 2 for all the models using the interpretations from the multichannel seismic image (Figure 11). It can be seen clearly that the 2D results show poor correlation with each other except at ~43 km where both models show unrealistically high velocities (Figure 11). However, the pattern of 2DA shows a match with the 3DB result in certain locations and the 2DB result shows a poor match with 3DB at all locations along the profile. None of the 2D results correlates well with the 3DA and 3DB results (Figure 11). The correlation between 3DA and 3DB is poor until ~27 km, beyond which the curves tend to follow each other. This mismatch between 3DA and 3DB in the western parts of the models may be due to inclusion of very limited data from OBSs 38 and 40. Moreover, the data from OBSs 38 and 40 were

limited to ~11 km offset because our starting model was not able to predict the data sufficiently well beyond these offsets for these OBSs. Only 10 shot profiles closest to their locations were included from these OBSs in 3DA and 3DB inversion runs.

Overlaying the 3DB velocity model over a time slice through the 3D seismic volume at 100 ms below an average depth of the S-reflector shows a good match between the velocity model and the time slice, suggesting that the model is well-resolved at these depths. The good match also suggests that, at the resolution of our models, the S-reflector is a velocity boundary (Figure 12). These observations suggest that 2D imaging has failed to generate a realistic model in the deeper parts. Furthermore, the range of velocities resolved by 3DB below the S-reflector indicates that 3DB has constrained the problem well with 8 km/s corresponding to unaltered peridotites with 0% serpentinisation (Carlson & Miller 2003). Velocities higher than 8.3 km/s are unrealistic at the S-reflector and lower velocities correspond to some degree of serpentinisation of the mantle (Bayrakci et al. 2016; Davy et al. 2018). In 3DB, the region below the S-reflector has been well resolved because of the data from the instruments located in the other OBS lines of the survey which were not included in the 2D and 2.5D inversion runs. Our 3D modelling has clearly enhanced resolution of the pattern of serpentinisation below the S-reflector compared to the starting model which predicted velocities mostly close to 6.5 km/s. Below the S-reflector the mantle peridotites have undergone serpentinisation, with an inferred maximum serpentinisation of 45% occurring around the fault intersections based on the relationship of Carlson & Miller (2003).

Based on 2DA, Davy et al. (2018) supported the concept of preferential serpentinisation of the upper mantle rocks close to faults. The result from 3DB along the same profile shows a better correlation between the fault intersections with the S-reflector and occurrence of lower velocities compared to the other models along this line.

5.3 Data fit

Another interesting aspect to compare between 2D and 3D FWI is the fit between the observed and predicted datasets. Our forward modelling scheme does not account for medium properties like anelastic attenuation and anisotropy, nor elastic and density effects that affect wave propagation in the real earth. Therefore, our modelling does not completely predict the field data, especially the amplitudes of the waveforms. Although technically it is possible to invert for these effects during an inversion, such an approach can make the inversion an ill-posed problem with many unknowns, particularly in case of a sparse OBS dataset with limited data coverage.

Wave propagation in 3D is more accurate than in 2D. Therefore, it can be expected that 3D waveforms fit the real data better than 2D waveforms. However, our data fitting results suggest that this expectation is not always met. We plotted data residuals for 2DB, 3DA and 3DB (2D, 2.5D and 3D, respectively) using data only used for the 2DB inversion (Appendix C). We applied trace-by-trace normalisation to the real and synthetic data before calculating the residuals. We calculated the data residuals for each model by subtracting the final model predicted data from the observed data and the RMS value of the difference was computed to quantify the fit in all three cases. For majority of the OBSs the fit between the predicted and observed data for the 2D and 3D cases is similar, and there are a few cases where 2D fits the data better than 3D (Figure 13). OBSs 38, 40, 81 and 82 show significantly better fits in 2D than in 3D. To explain these observations, we explore the cases of instruments 45, 46 and 38 in detail.

For OBS 45, the 2D inversion provides the best fit, while for OBS 46, the 2.5D inversion provides the best fit (Figure 14). The differences are small, making it difficult to establish clearly which inversion is better fitting the data. We performed 30 iterations at each frequency in all the inversions and increasing the number of iterations may have further narrowed the

differences without significant improvements in the velocity models. However, for OBS 38, the differences between 2D, 2.5D and 3D cases are significant compared to other OBSs (Figure 14). OBS 38 has high uncertainty in its location due to the need to correct large time shifts in the raw data, so only very limited data from this OBS, that our starting model was able to predict, were used in the inversion. The significantly smaller RMS value of 2D residuals compared to 2.5D and 3D residuals may be due to overfitting. It is possible that there is overfitting in all the three cases for all the OBSs. However, the degree of overfitting varies from OBS to OBS depending on various factors that affect the constraints on the inversion such as the dimensions of the problem, data sparsity, OBS location uncertainties and unaccounted wave propagation effects. We suspect higher degrees of overfitting of data in the 2D case in OBSs 38, 40, 81 and 82 which show larger differences in the RMS values of the residuals (Figure 13). It is also possible that the circular features observed in the 2D imaging partially resulted from overfitting. The difference between 2.5D and 3D RMS values is due to the inclusion of the data from the OBSs along lines 1 and 3 resulting in lesser constraints on the 2.5D inversion compared to the 3D inversion (Figure 2).

In our comparison of data residuals, it is important to note is that we have suppressed the amplitude effects during the inversion by performing trace normalisation of the datasets. Inverting for amplitude effects would have probably resulted in larger data residuals, fundamentally due to the different 2D and 3D forward modelling operators. Even with such subtle differences in the data residuals, an interesting observation is the occurrence of brighter residuals at the near offsets in the 3D data residuals (Figure 14). This is probably due to poor sampling of the subsurface by OBS data in the near offsets in general, perhaps sparse spacing between the OBS may have further reduce the constraints at the near offsets. However, the same near-offset arrivals in the 2D data residuals are matched due to overfitting by the inversion (Figure 14).

6. Recovering the anomalies

The most common way to estimate the resolution of the final inverted model is through checkerboard tests (e.g. Morgan et al. 2016). In our case, we did not perform checkerboard tests because introducing even small anomalies in the form of checkers resulted in changing of the arrival times, particularly far-offset arrivals, beyond the range of our mute gates applied to the input data for the actual inversion. Instead, we added the anomalies introduced by the FWI into the starting model and recovered the anomalies by performing synthetic tests. To check whether our inversion strategies produced consistent results and to explore the size of the anomalies introduced by the FWI, and hence the resolution of the inversions, we performed synthetic inversion runs using the 2DB, 3DA and 3DB models. In these tests, we generated synthetic data using the final models and used the synthetic data as observed data in the inversion runs. The synthetic data were generated using the same forward modelling scheme as used in the actual inversion runs. The starting model was the same as used in the actual runs (Bayrakci et al 2016). The results from these inversions, when subtracted from the starting should match the anomalies recovered in the actual inversion runs 2DB, 3DA and 3DB (Figure 14). All three tests successfully recovered most of the anomalies introduced by the FWI into the final models, indicating that the anomalies recovered in the actual inversion runs are real. However, the amplitudes of the recovered anomalies are smaller in magnitude than the actual anomalies. This discrepancy may be because of employing trace-by-trace normalised misfit function in the inversion which in effect only inverts for phase information in the data. The RMS amplitudes of the differences between the anomalies introduced by FWI and the anomalies recovered are 45 m/s, 68 m/s and 83 m/s for the 2DB, 3DA and 3DB inversions, respectively.

Analysing the anomalies introduced by 2D, 2.5D and 3D inversion, we observe that the shapes of anomalies introduced by 2DB differ from 3DA and 3DB. This difference is due many factors

affecting the constraints on the inverse problem with major contribution coming from the difference in the amount of data. An interesting change in the anomalies from 2D to 3D is the extent of the blue anomaly below the S-reflector (Figure 15). In 2DB, the blue anomaly below S is mainly observed between ~35 and 50 km, while in 3DA and 3DB the anomaly extends to ~27 km and ~20 km, respectively, covering the full length of the S in 3DB (Figure 15). This progressive extension of the anomaly demonstrates that 2DB failed to resolve the velocities below the S-reflector along its full length. The reason for the poor performance of 2DB below the S-reflector may be that fewer first arrivals from these regions are included in the inversion. This problem may be a more general one for performing FWI on sparsely recorded datasets. Previously, most 2D FWI studies using OBS datasets have had advantage of close spacing of the OBS and long offset recording, enabling strong constraints on the deeper part (e.g. Dessa et al. 2004; Operto et al. 2006). Jian et al. (2017) demonstrated the application of 2D elastic FWI to a sparely recorded OBS dataset to image an axial magma chamber-like structure below the Southwest Indian Ridge. In that study, data from only three OBSs were used and the spacing between the OBSs were 8 km and 16 km, which is greater than in our study. However, in spite of such sparse spacing, FWI successfully converged using data from offsets up to ~50 km. Combining the experience from this and previous studies of FWI implementation using OBS data, it can be inferred that OBS spacing is an important factor for successful application of FWI, but other factors are also important, such as shot spacing, the maximum offset with usable data and the target depth of investigation. In our case, the 3D dataset has partly mitigated the problem of data sparsity, which is evident from the differences between the 2D and 3D FWI results.

7. Conclusions

We have successfully performed 3D FWI in the time domain using wide-angle data recorded using sparsely spaced OBSs on the Deep Galicia margin. We compared our results with a 2D

FWI result derived using a subset of the dataset through the 3D model. Our comparison revealed:

1. Both 2D and 3D FWI applications show improved alignment of the structures with coincident multichannel seismic reflection images, compared to the travel-time model.
2. Within the pre- and syn-rift sediments, the 2D model shows an oscillatory behaviour, which is reduced in the 3D model indicating 3D nature of the fine-scale faulting.
3. In the crystalline crust, 2D imaging fails to fully recover the alignment of structures due to the complex 3D nature of the faults observed on the multichannel reflection images.
4. Poor constraints on the inverse problem due to sparse data and/or our assumed approximation of the wave equation results in circular velocity contours which are geologically unrealistic. 2D FWI images contained more such features than 3D images, indicating that they arise mainly from the data sparseness.
5. The 3D FWI model has enhanced the resolution of the pattern of serpentinisation below the S-reflector compared to the starting model. The occurrence of lower velocities below the S-reflector correlates with overlying fault intersections at the S-reflector.
6. Data residual plots suggest that 2D inversion can be prone to overfitting in the case of a sparse OBS dataset, while 2.5D and 3D inversions are better constrained with more data to avoid overfitting. Overfitting may vary from OBS to OBS depending on factors like location uncertainty and poor coverage by the data.
7. Anomaly recovery tests recovered the anomalies introduced by the FWI in both 2D and 3D. The progressive extension of an anomaly below the S from 2D to 3D results highlights that the 2D inverse problem is poorly constrained in the deeper parts of the model.

8. Acknowledgements

Data acquisition was supported by the U.S. National Science Foundation, the UK Natural Environment Research Council (NERC; grant NE/E016502/1), and GEOMAR. Ocean bottom instrumentation was provided by the NERC UK Ocean Bottom Instrumentation Facility and by GEOMAR. T.A.M. was supported by a Wolfson Research Merit award. The 3D ProMAX/SeisSpace package, supplied by Halliburton under a university software grant, was used to preprocess and analyse the field data within University of Southampton. We thank Jeff Blundell at the University of Southampton for assisting in setting up the code on supercomputing facilities. We thank the members of the Fullwave research consortium at Imperial College London who funded the development of the FWI software used in this study. We thank Richard Davy for providing his 2D FWI result and Gael Lymer for providing his interpretations of the 3D reflection volume. We thank Milena Marjanović, Andrzej Górszczyk and other anonymous reviewers for providing constructive reviews and comments that greatly improved the manuscript. We thank the editor Michal Malinowski for suggesting improvements to the manuscript.

Data Availability:

The data underlying this article are being uploaded to https://www.pangaea.de. Prior to availability there, they will be shared on a reasonable request to the corresponding author

9. References

Bayrakci, G., Minshull, T. A., Sawyer, D. S., Reston, T. J., Klaeschen, D., Papenberg, C., et al. (2016). Fault-controlled hydration of the upper mantle during continental rifting.

662 *Nature Geoscience*, *9*(5), 384–388. https://doi.org/10.1038/ngeo2671
663 Beslier, M. O., Ask, M., & Boillot, G. (1993). Ocean-continent boundary in the Iberia Abyssal
664 Plain from multichannel seismic data. *Tectonophysics*, *218*(4), 383–393.
665 https://doi.org/10.1016/0040-1951(93)90327-G
666 Boillot, G., Grimaud, S., Mauffret, A., Mougenot, D., Kornprobst, J., Mergoil-Daniel, J., &
667 Torrent, G. (1980). Ocean-continent boundary off the Iberian margin: A serpentinite
668 diapir west of the Galicia Bank. *Earth and Planetary Science Letters*, *48*(1), 23–34.
669 https://doi.org/10.1016/0012-821X(80)90166-1
670 Boillot, G., Winterer, E. L., & Meyer, A. W. (1987). Ocean Drill. Program Initial Rep.,103.
671 *Ocean Drilling Program, College Station, TX*.
672 Boillot, Gilbert, & Winterer, E. L. (1988). *DRILLING ON THE GALICIA MARGIN: RETROSPECT*
673 *AND PROSPECT*. *Proceedings of the Ocean Drilling Program, Scientific Results*.
674 Bunks, C., Saleck, F. M., Zaleski, S., & Chavent, G. (1995). Multiscale seismic waveform
675 inversion. *Geophysics*, *60*(5), 1457–1473. https://doi.org/10.1190/1.1443880
676 Carlson, R. L., & Miller, D. J. (2003). Mantle wedge water contents estimated from seismic
677 velocities in partially serpentinized peridotites. *Geophysical Research Letters*, *30*(5),
678 n/a-n/a. https://doi.org/10.1029/2002gl016600
679 De Charpal, O., Guennoc, P., Montadert, L., & Roberts, D. G. (1978). Rifting, crustal
680 attenuation and subsidence in the Bay of Biscay. *Nature*, *275*(5682), 706–711.
681 https://doi.org/10.1038/275706a0
682 Davy, R. G., Minshull, T. A., Bayrakci, G., Bull, J. M., Klaeschen, D., Papenberg, C., et al.
683 (2016). Continental hyperextension, mantle exhumation, and thin oceanic crust at the
684 continent-ocean transition, West Iberia: New insights from wide-angle seismic. *Journal*
685 *of Geophysical Research : Solid Earth*, 1–17.

686 https://doi.org/10.1002/2016JB012825.Received
687 Davy, R. G., Morgan, J. V., Minshull, T. A., Bayrakci, G., Bull, J. M., Klaeschen, D., et al. (2018).
688 Resolving the fine-scale velocity structure of continental hyperextension at the Deep
689 Galicia Margin using full-waveform inversion. *Geophysical Journal International*, *212*(1),
690 244–263. https://doi.org/10.1093/gji/ggx415
691 Dean, S. L., Sawyer, D. S., & Morgan, J. K. (2015). Galicia Bank ocean-continent transition
692 zone: New seismic reflection constraints. *Earth and Planetary Science Letters*, *413*,
693 197–207. https://doi.org/10.1016/j.epsl.2014.12.045
694 Dessa, J. X., Operto, S., Kodaira, S., Nakanishi, A., Pascal, G., Virieux, J., & Kaneda, Y. (2004).
695 Multiscale seismic imaging, of the eastern Nankai trough by full waveform inversion.
696 *Geophysical Research Letters*, *31*(18), 2–5. https://doi.org/10.1029/2004GL020453
697 Gardner, G. H. F., Gardner, L. W., & Gregory, A. R. (1974). Formation velocity and density -
698 The diagnostic basics for stratigraphic traps, *39*(6), 770–780.
699 Górszczyk, A., Operto, S., & Malinowski, M. (2017). Toward a robust workflow for deep
700 crustal imaging by FWI of OBS data: The eastern Nankai Trough revisited. *Journal of*
701 *Geophysical Research: Solid Earth*, *122*(6), 4601–4630.
702 https://doi.org/10.1002/2016JB013891
703 Górszczyk, A., Operto, S., Schenini, L., & Yamada, Y. (2019). Crustal-scale depth imaging via
704 joint FWI of OBS data and PSDM of MCS data: a case study from the eastern Nankai
705 Trough. *Solid Earth Discussions*, 1–34. https://doi.org/10.5194/se-2019-33
706 Hammer, P. T. C., Dorman, L. M., Hildebrand, J. A., & Cornuelle, B. D. (1994). Jasper
707 Seamount structure: seafloor seismic refraction tomography. *Journal of Geophysical*
708 *Research*, *99*(B4), 6731–6752. https://doi.org/10.1029/93JB02170
709 Jian, H., Singh, S. C., Chen, Y. J., & Li, J. (2017). Evidence of an axial magma chamber beneath

the ultraslowspreading Southwest Indian Ridge. *Geology*, *45*(2), 143–146. https://doi.org/10.1130/G38356.1

Kamei, R., Pratt, R. G., & Tsuji, T. (2013). On acoustic waveform tomography of wide-angle OBS data-strategies for pre-conditioning and inversion. *Geophysical Journal International*, *194*(2), 1250–1280. https://doi.org/10.1093/gji/ggt165

Lailly, P. (1983). The Seismic Inverse Problem as a Sequence of Before Stack Migrations. In *Conference on Inverse Scattering, Theory and Applications, Society for Industrial and Applied Mathematics* (pp. 206–220).

Leythaeuser, T., Reston, T. J., & Minshull, T. A. (2005). Waveform inversion of the S reflector west of Spain: Fine structure of a detachment fault. *Geophysical Research Letters*. https://doi.org/10.1029/2005GL024026

Lines, L. R., Slawinski, R., & Bording, R. P. (1999). A recipe for stability of finite-difference wave-equation computations. *Geophysics*, *64*(3), 967–969. https://doi.org/10.1190/1.1444605

Lymer, G., Cresswell, D. J. F., Reston, T. J., Bull, J. M., Sawyer, D. S., Morgan, J. K., et al. (2019). 3D development of detachment faulting during continental breakup. *Earth and Planetary Science Letters*, *515*, 90–99. https://doi.org/10.1016/j.epsl.2019.03.018

Morgan, J., Warner, M., Arnoux, G., Hooft, E., Toomey, D., VanderBeek, B., & Wilcock, W. (2016). Next-generation seismic experiments - II: Wide-angle, multi-azimuth, 3-D, full-waveform inversion of sparse field data. *Geophysical Journal International*, *204*(2), 1342–1363. https://doi.org/10.1093/gji/ggv513

Murillas, J., Mougenot, D., Boulot, G., Comas, M. C., Banda, E., & Mauffret, A. (1990). Structure and evolution of the Galicia Interior Basin (Atlantic western Iberian continental margin). *Tectonophysics*, *184*(3–4). https://doi.org/10.1016/0040-

734 1951(90)90445-E
735 Operto, S., Virieux, J., Dessa, J. X., & Pascal, G. (2006). Crustal seismic imaging from multifold
736 ocean bottom seismometer data by frequency domain full waveform tomography:
737 Application to the eastern Nankai trough. *Journal of Geophysical Research: Solid Earth*,
738 *111*(9), 1–33. https://doi.org/10.1029/2005JB003835
739 Paige, C. C., & Saunders, M. A. (1982). LSQR: An Algorithm for Sparse Linear Equations and
740 Sparse Least Squares. *ACM Transactions on Mathematical Software (TOMS)*, *8*(2), 195–
741 209. https://doi.org/10.1145/355993.356000
742 Pérez-Gussinyé, M., Ranero, C. R., Reston, T. J., & Sawyer, D. (2003). Mechanisms of
743 extension at nonvolcanic margins: Evidence from the Galicia interior basin, west of
744 Iberia. *Journal of Geophysical Research: Solid Earth*, *108*(B5), 1–19.
745 https://doi.org/10.1029/2001JB000901
746 Pérez-Gussinyé, Marta, & Reston, T. J. (2001). Rheological evolution during extension at
747 nonvolcanic rifted margins: Onset of serpentinization and development of detachments
748 leading to continental breakup. *Journal of Geophysical Research: Solid Earth*, *106*(B3),
749 3961–3975. https://doi.org/10.1029/2000jb900325
750 Péron-Pinvidic, G., Manatschal, G., Minshull, T. A., & Sawyer, D. S. (2007).
751 Tectonosedimentary evolution of the deep Iberia-Newfoundland margins: Evidence for
752 a complex breakup history. *Tectonics*, *26*(2), 1–19.
753 https://doi.org/10.1029/2006TC001970
754 Pratt, R. G., Song, Z. M., Williamson, P., & Warner, M. (1996). Two-dimensional velocity
755 models from wide-angle seismic data by wavefield inversion. *Geophysical Journal*
756 *International*, *124*(2), 323–340. https://doi.org/10.1111/j.1365-246X.1996.tb07023.x
757 Ranero, C. R., & Pérez-Gussinyé, M. (2010). Sequential faulting explains the asymmetry and

758 extension discrepancy of conjugate margins. *Nature*, *468*(7321), 294–299.
759 https://doi.org/10.1038/nature09520
760 Reston, T. J. (2005). Polyphase faulting during the development of the west Galicia rifted
761 margin. *Earth and Planetary Science Letters*, *237*(3–4), 561–576.
762 https://doi.org/10.1016/j.epsl.2005.06.019
763 Reston, T. J. (2007). The formation of non-volcanic rifted margins by the progressive
764 extension of the lithosphere: the example of the West Iberian margin. *Geological*
765 *Society, London, Special Publications*, *282*(1), 77–110. https://doi.org/10.1144/SP282.5
766 Reston, T. J. (2009). The structure, evolution and symmetry of the magma-poor rifted
767 margins of the North and Central Atlantic: A synthesis. *Tectonophysics*, *468*(1–4), 6–27.
768 https://doi.org/10.1016/j.tecto.2008.09.002
769 Reston, T. J., Krawczyk, C. M., & Klaeschen, D. (1996). The S reflector west of Galicia (Spain):
770 Evidence from prestack depth migration for detachment faulting during continental
771 breakup. *Journal of Geophysical Research: Solid Earth*, *101*(B4), 8075–8091.
772 https://doi.org/10.1029/95JB03466
773 Reston, T. J., Booth-Rea, G., Leythaeuser, T., Sawyer, D., Klaeschen, D., & Long, C. (2007).
774 Movement along a low-angle normal fault: The S reflector west of Spain. *Geochemistry,*
775 *Geophysics, Geosystems*, *8*(6), 1–14. https://doi.org/10.1029/2006GC001437
776 Schuba, C. N., Gray, G. G., Morgan, J. K., Sawyer, D. S., Shillington, D. J., Reston, T. J., et al.
777 (2018). A low-angle detachment fault revealed: Three-dimensional images of the S-
778 reflector fault zone along the Galicia passive margin. *Earth and Planetary Science*
779 *Letters*, *492*, 232–238. https://doi.org/10.1016/j.epsl.2018.04.012
780 Shah, N., Warner, M., Nangoo, T., Umpleby, A., Stekl, I., Morgan, J., & Guasch, L. (2012).
781 Quality assured full-waveform inversion: Ensuring starting model adequacy. In *81st*

Annual International Meeting, SEG, Expanded abstract, SI3.5. (pp. 1–5).

Sirgue, L. (2006). The importance of low frequency and large offset in waveform inversion. In *68th EAGE Conference and Exhibition incorporating SPE EUROPEC 2006*.

Srivastava, S. P., Sibuet, J. C., Cande, S., Roest, W. R., & Reid, I. D. (2000). Magnetic evidence for slow seafloor spreading during the formation of the Newfoundland and Iberian margins. *Earth and Planetary Science Letters*, *182*(1), 61–76. https://doi.org/10.1016/S0012-821X(00)00231-4

Tarantola, A. (1984). Inversion of seismic reflection data in the acoustic approximation. *Geophysics*, *49*(8), 1259–1266. https://doi.org/10.1190/1.1441754

Tucholke, B. E., Sawyer, D. S., & Sibuet, J.-C. (2007). Breakup of the Newfoundland Iberia rift. *Geological Society, London, Special Publications*, *282*(1), 9–46. https://doi.org/10.1144/SP282.2

Warner, M., Ratcliffe, A., Nangoo, T., Morgan, J., Umpleby, A., Shah, N., et al. (2013). Anisotropic 3D full-waveform inversion. *Geophysics*, *78*(2), R59–R80. https://doi.org/10.1190/geo2012-0338.1

Whitmarsh, R. B., Manatschal, G., & Minshull, T. A. (2001). Evolution of magma-poor continental margins from rifting to seafloor spreading. *Nature*, *413*(6852), 150–154. https://doi.org/10.1038/35093085

Zelt, C. A., & Barton, P. J. (1998). Three-dimensional seismic refraction tomography: A comparison of two methods applied to data from the Faraoe Basin. *J. Geophys. Res.*, *103*(B4), 7187–7210.

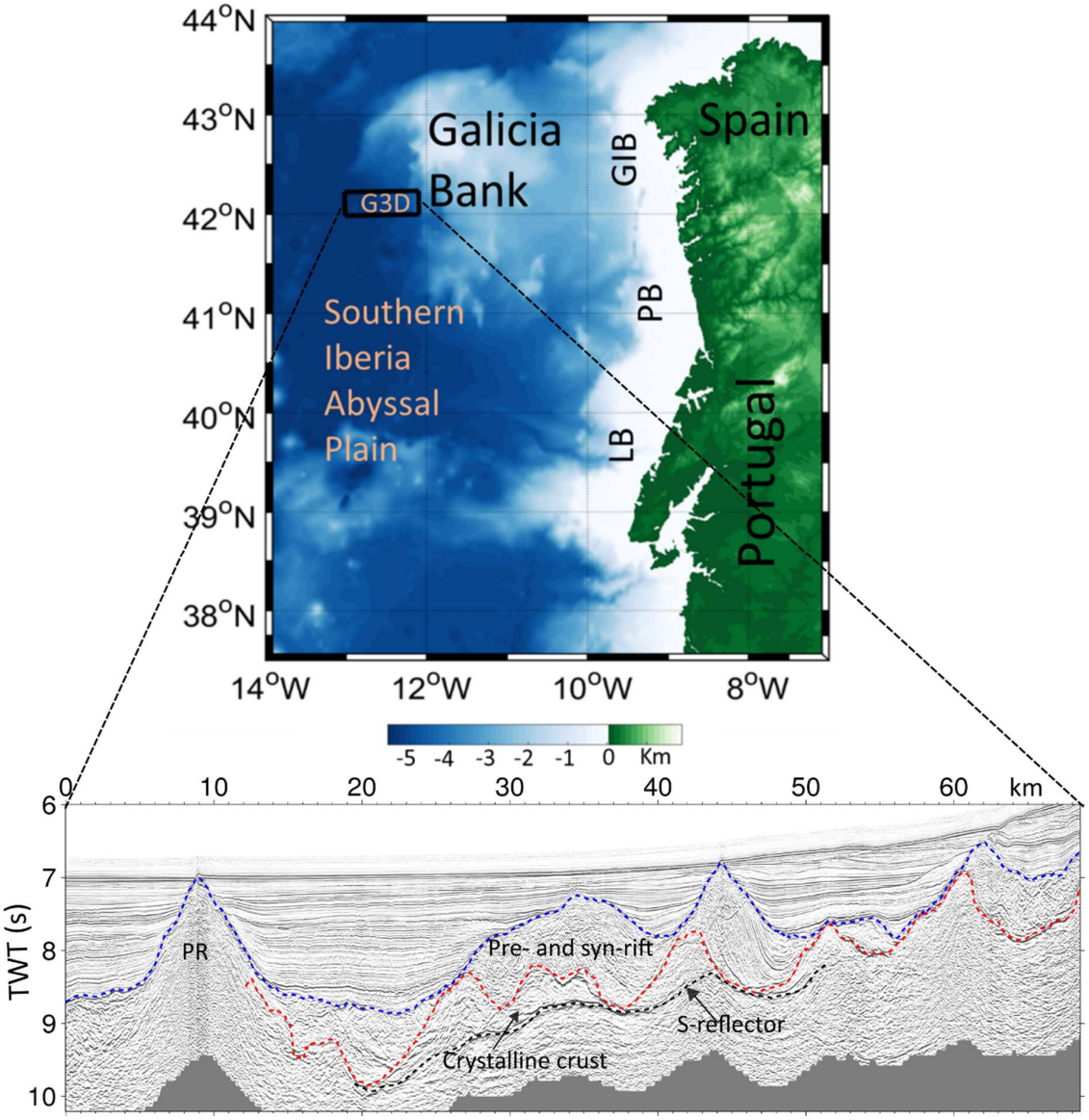

Figure 1 | Upper panel: map showing the location of the Galicia 3D (G3D) experiment in the DGM (black box). East of the DGM is the Galicia Bank, Galicia Interior Basin (GIB), Porto Basin (PB) and Lusitania Basin (LB). To the south of the study region is the Southern Iberia Abyssal Plain. Colours in the map indicate bathymetry and topography. Lower panel: time migrated seismic profile across G3D area highlighting the Peridotite Ridge (PR), pre- and syn-rift sediments (below dashed blue), crystalline crust (below dashed red) and the S-reflector (dashed black).

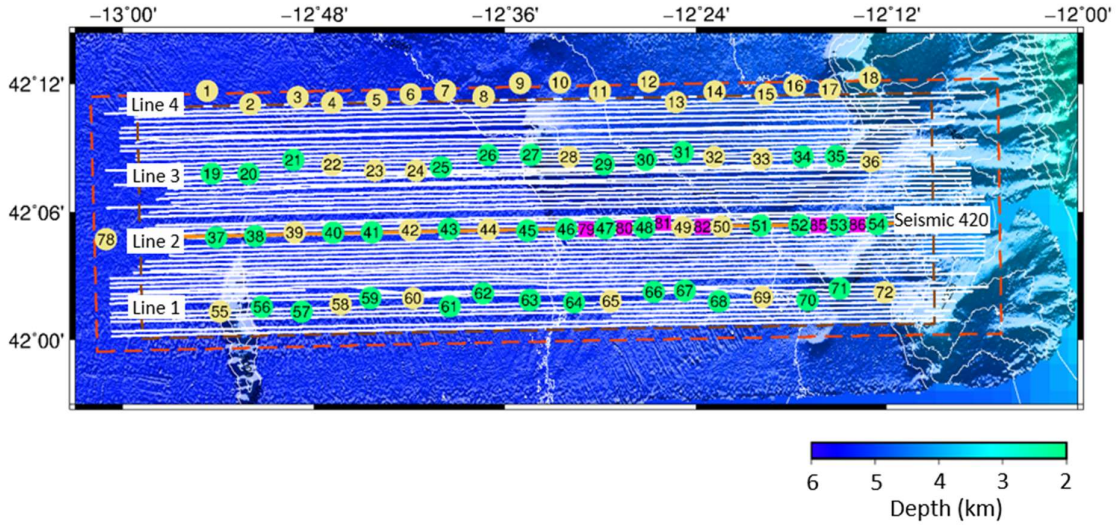

Figure 2 | Map showing the location of the OBSs, and multichannel seismic shooting in white. The OBSs locations are indicated along four profiles from south to north: line1, line2 line3 and line4. Locations of multichannel seismic line 420 through the instruments in line2 is shown in orange. The red-dashed box marks the area for the 3D FWI and the dashed brown box marks the multichannel seismic volume. Green coloured instruments are used for 3D FWI, whereas the yellow ones have not been used in this work. The instruments in pink have only two shot profiles recorded directly above them.

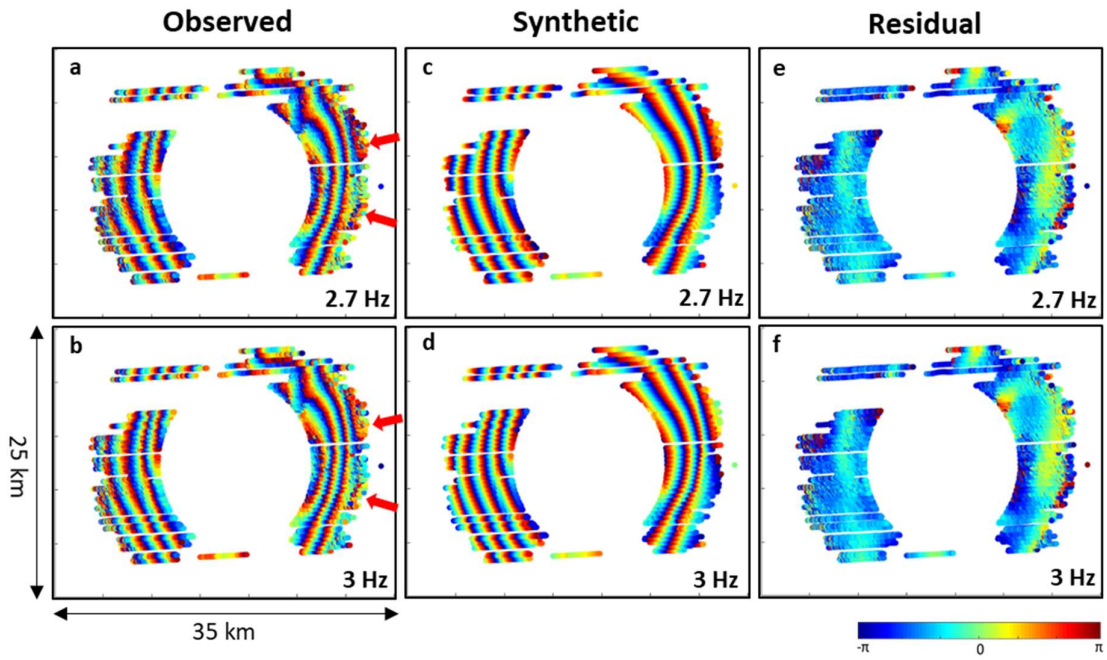

Figure 3 | Phase residuals for OBS 46 for the starting model at frequencies 2.7 Hz and 3 Hz. Each dot represents the phase of the first arrivals extracted using a Gaussian window centred on these arrivals. a) & b) are the phase plots of the observed data at 2.7 and 3 Hz, respectively. c) & d) are the phase plots of the synthetic data predicted using the starting model at 2.7 and 3 Hz, respectively. The residual plot (e & f) indicate that most of the data is predicted within half a cycle accuracy by the starting model. Noisy traces at far offsets indicated by red arrows are out of phase.

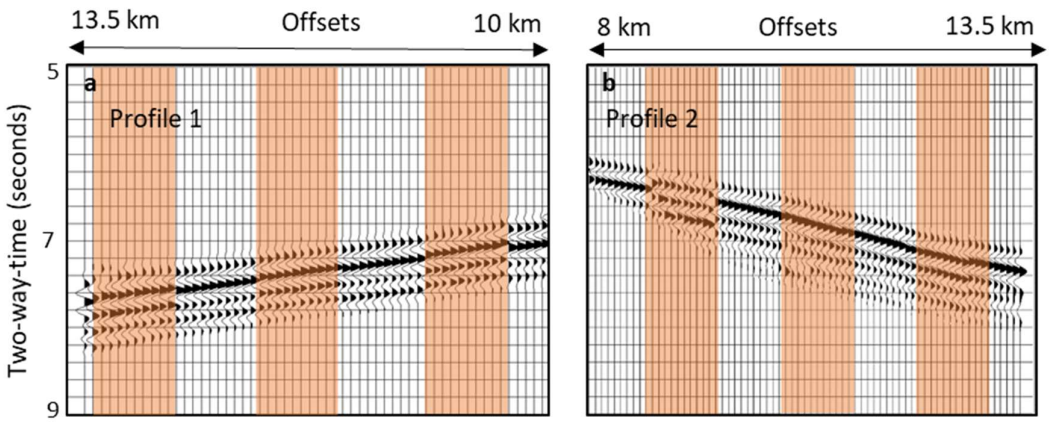

872
873
874 **Figure 4** | Observed (highlighted) and predicted data using the starting model plotted in sets of 10 traces
875 from OBS 46, alternating to show the match between the arrivals along two profiles. a) Profile 1 is the
876 closest profile to the OBS 46 location and b) Profile 2 is at a distance of ~10 km from this location. The
877 data shown are band-pass filtered and trace-by-trace normalised.
878

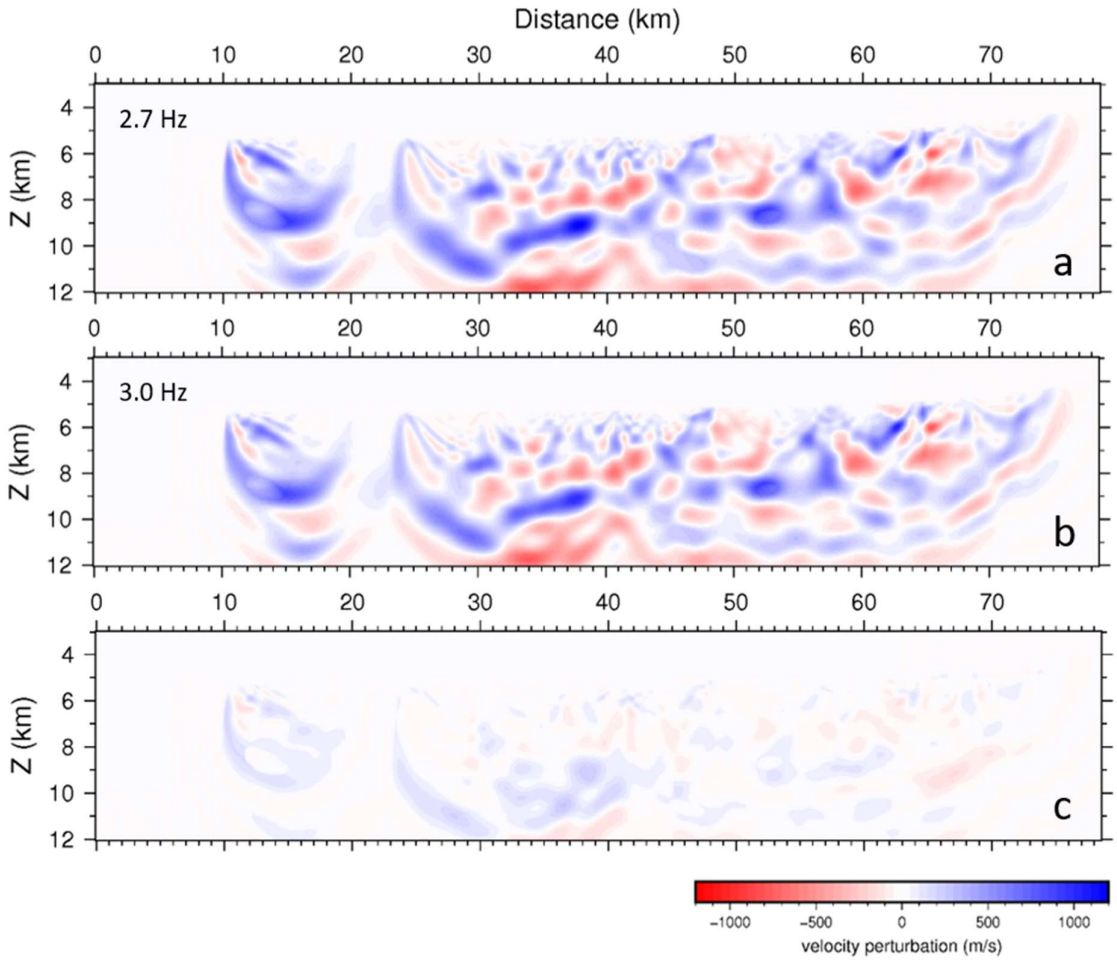

Figure 5 | Difference between the starting model and final model along a profile through the instruments in line 2 using the 3D inversion. a) is the difference plot for inversion starting from 2.7 Hz and b) is the difference plot for inversion starting from 3Hz. c) is the difference between a) and b).

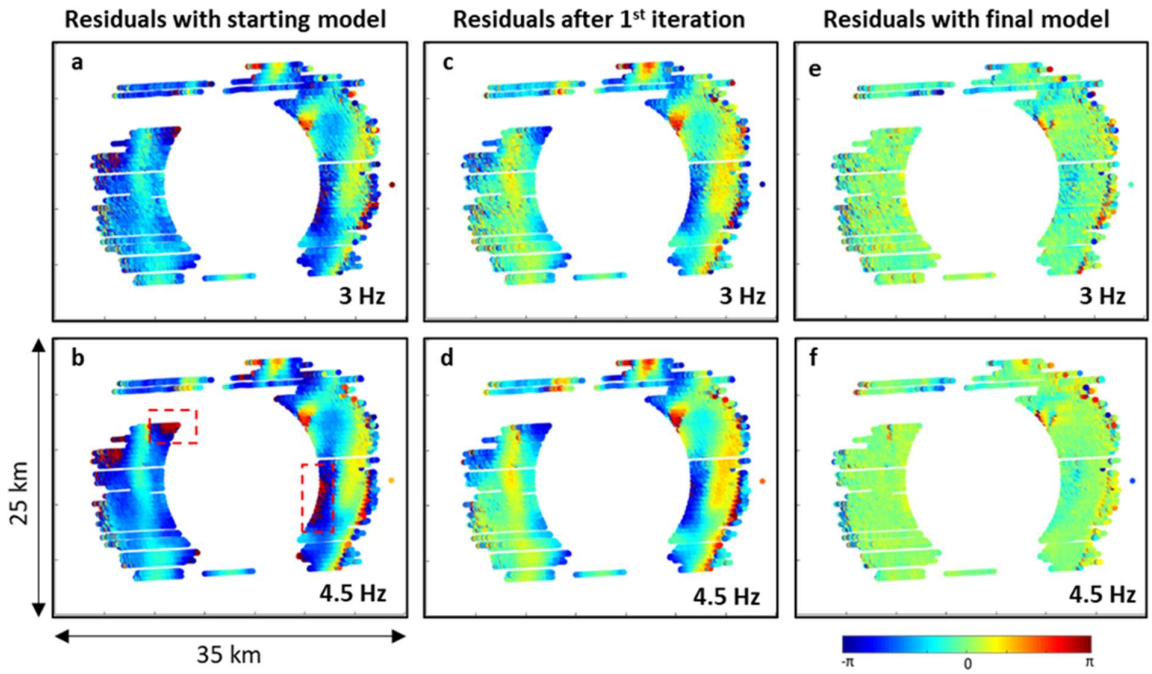

Figure 6 | Phase plots residuals for starting model, model after 1st iteration and final models at 3 and 4.5 Hz. The phases show gradual change towards zero phase difference except at two locations highlighted in dashed red boxes at 4.5 Hz. A few lines have been excluded from the inversion because of their poor fit or poor quality, resulting in gaps in the refracted arrivals in the above plots.

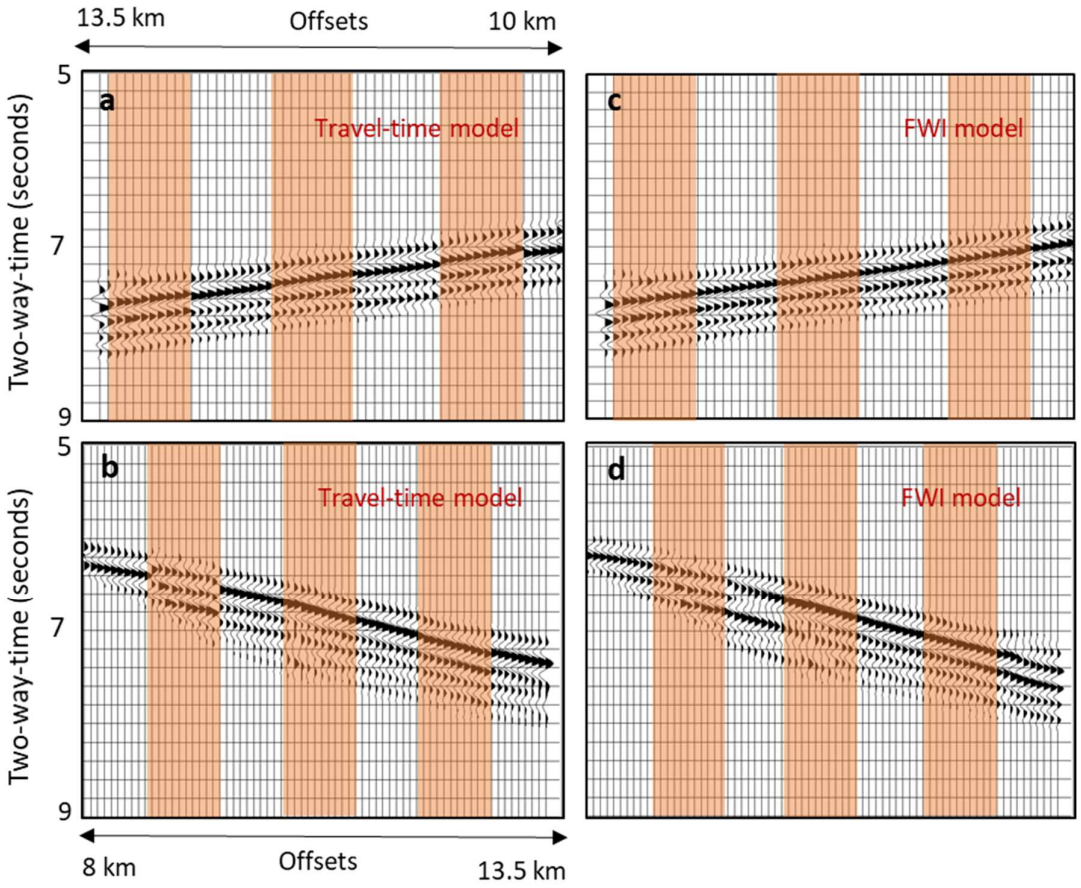

Figure 7 | Observed and synthetic data along the same two profiles from OBS 46 as shown in Figure 4. a) and b) Left-hand profiles are alternating sets of 10 traces from observed data (highlighted) and synthetics from the starting model. c) and d) Right-hand plots show the observed data (highlighted) and synthetics from the final model.

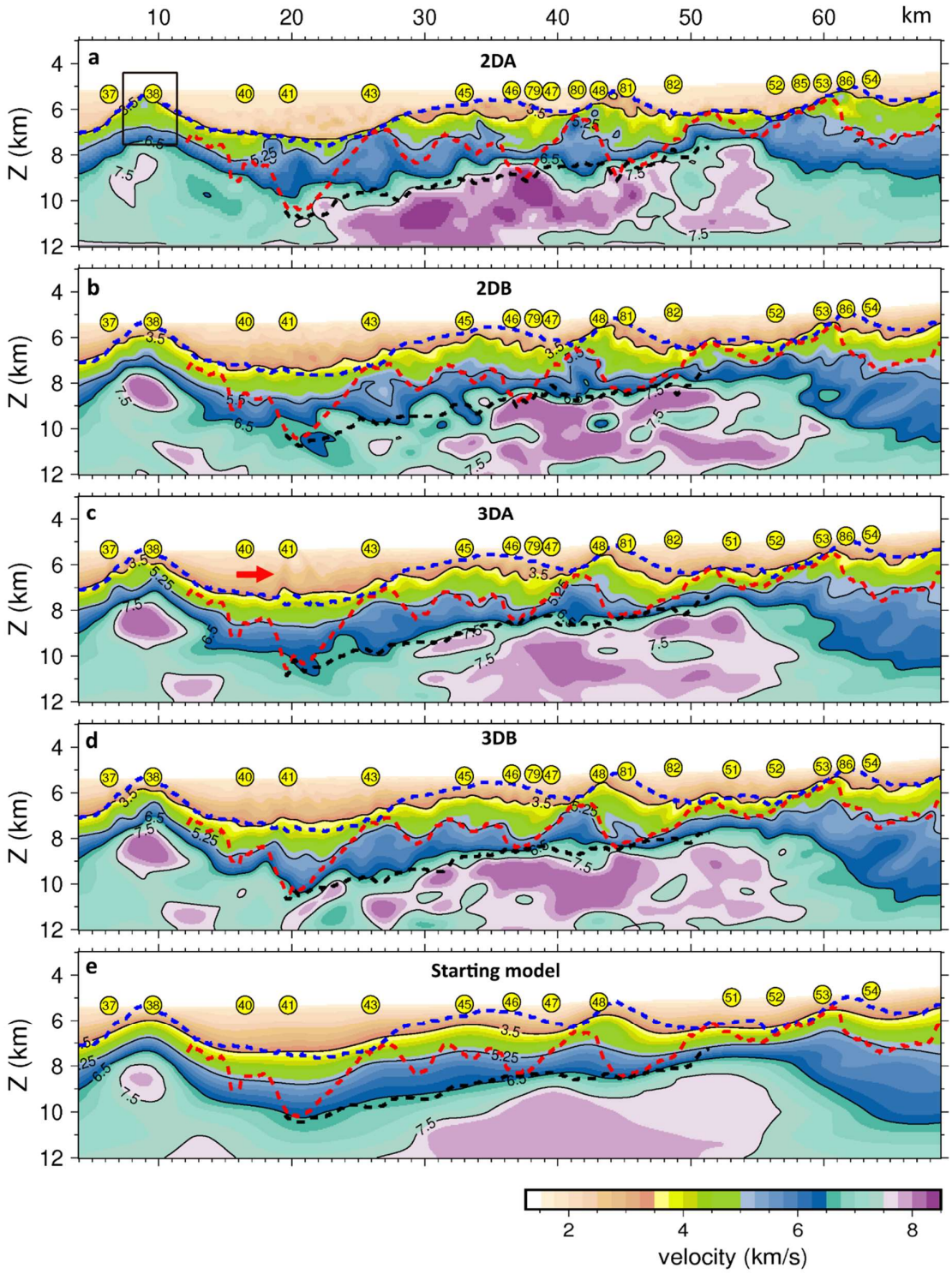

939

940 **Figure 8** | Velocity profiles along line 2: Profile **a** is the result from 2D FWI – 2DA (Davy et al. 2018),
941 profile **b** is the 2D FWI from the 3D starting model – 2DB, profile **c** is the 3D FWI using only the
942 instruments along line 2 – 3DA, profile **d** is the result from the full 3D FWI using instruments coloured
943 in green and pink in figure 2, and profile **e** is the starting model from 3D travel-time tomography

(Bayrakci et al. 2016). Comparing the 2D FWI and 3D FWI in depth domain. Interpretations from multi-channel seismic images (Lymer et al. 2019) are converted from time to depth using respective velocity models and overlaid on the sections along with the OBS locations in yellow circles. Dashed blue line marks top of the syn-rift sediments, dashed red line is the top of the crystalline crust and dashed black line is the S-reflector. Velocity contours for 3.5, 5.25, 6.5 and 7.5 km/s are marked in solid black lines. The red arrow indicates imaging artefacts. The black solid box in 2DA around peridotite ridge highlights a good match between the multichannel interpretation (dashed blue) and the velocity contour for 3.5 km/s compared to the other models.

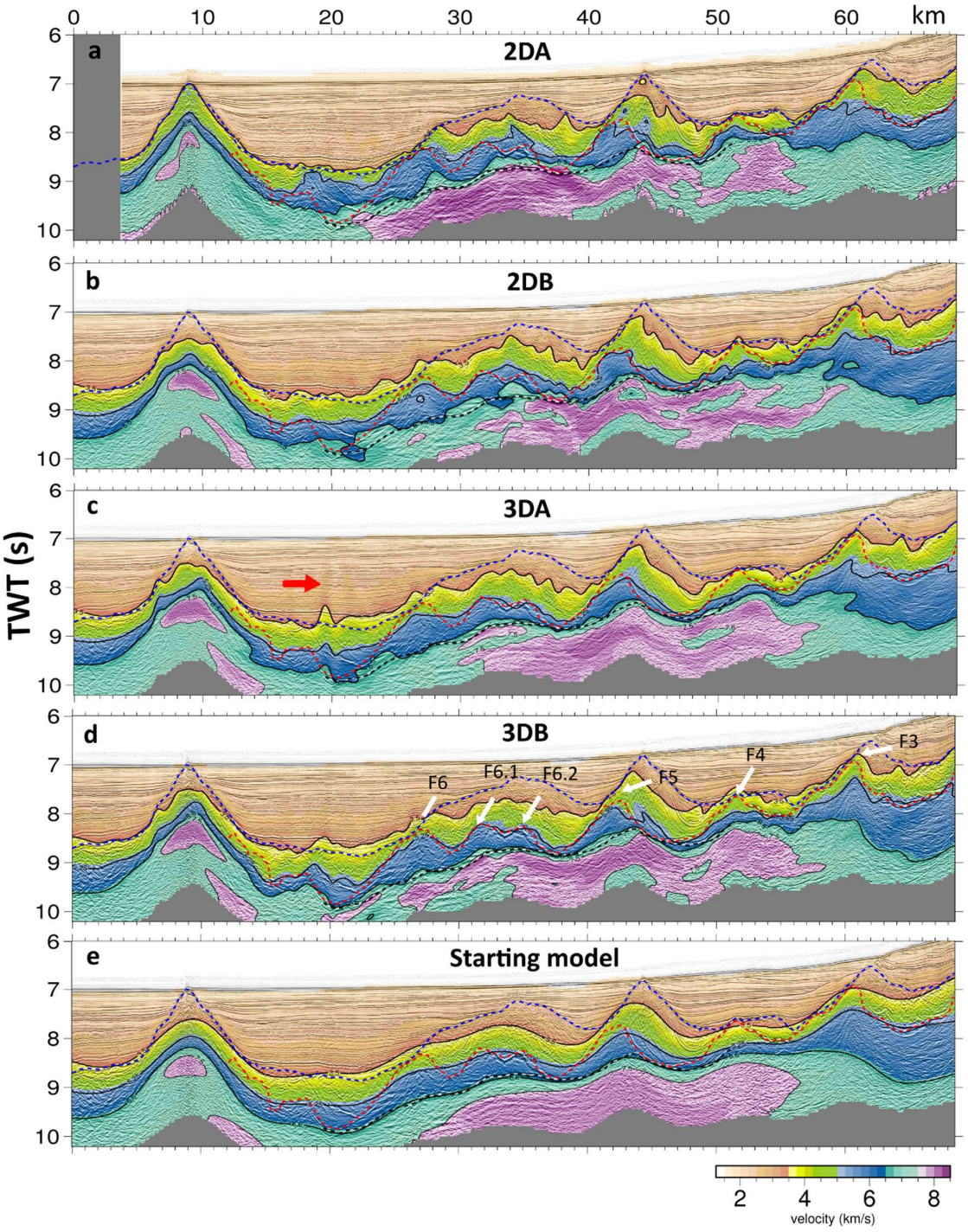

Figure 9 | Comparison between 2D and 3D FWI results and multichannel time sections, which are overlaid with interpretations from Lymer et al. (2019). Profiles and velocity contours correspond to their respective profile and contour labels in Figure 8. Fault numbers (F-series) are marked on the FWI result (**d**). Red arrow marks vertical artefacts.

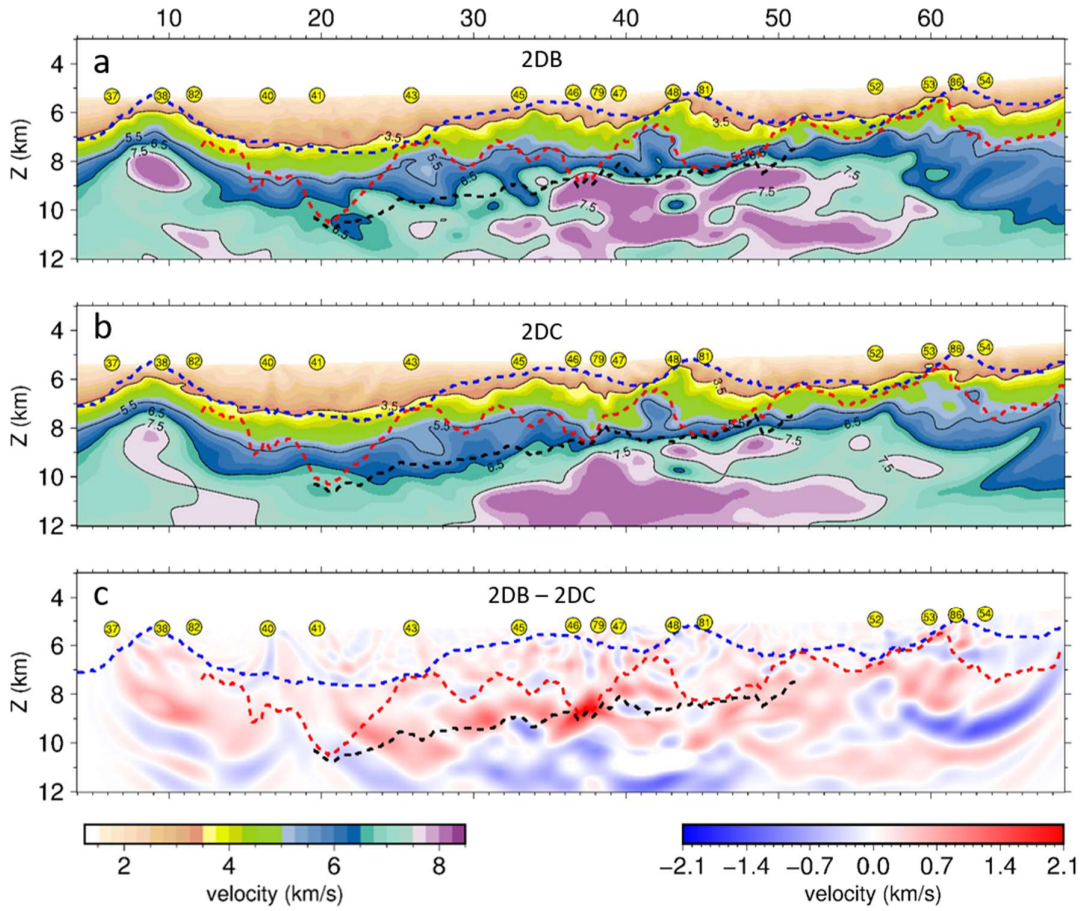

Figure 10 | 2D FWI inversion results a) 2DB obtained by projecting shots and receivers onto the imaging line b) 2DC performed using a narrow 3D grid encompassing the shots and receivers at their actual locations c) difference between 2DB and 2DC indicates that the differences are larger below 8 km depth.

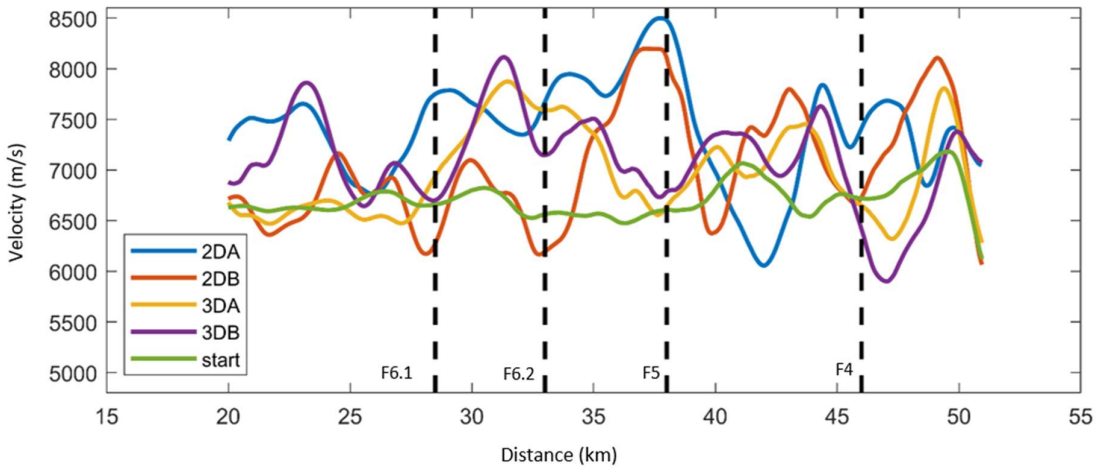

Figure 11 | Velocities below the S-reflector averaged over a window of 100 ms for each of the FWI results. The intersection of the faults with the S-reflector are indicated by vertical dashed lines.

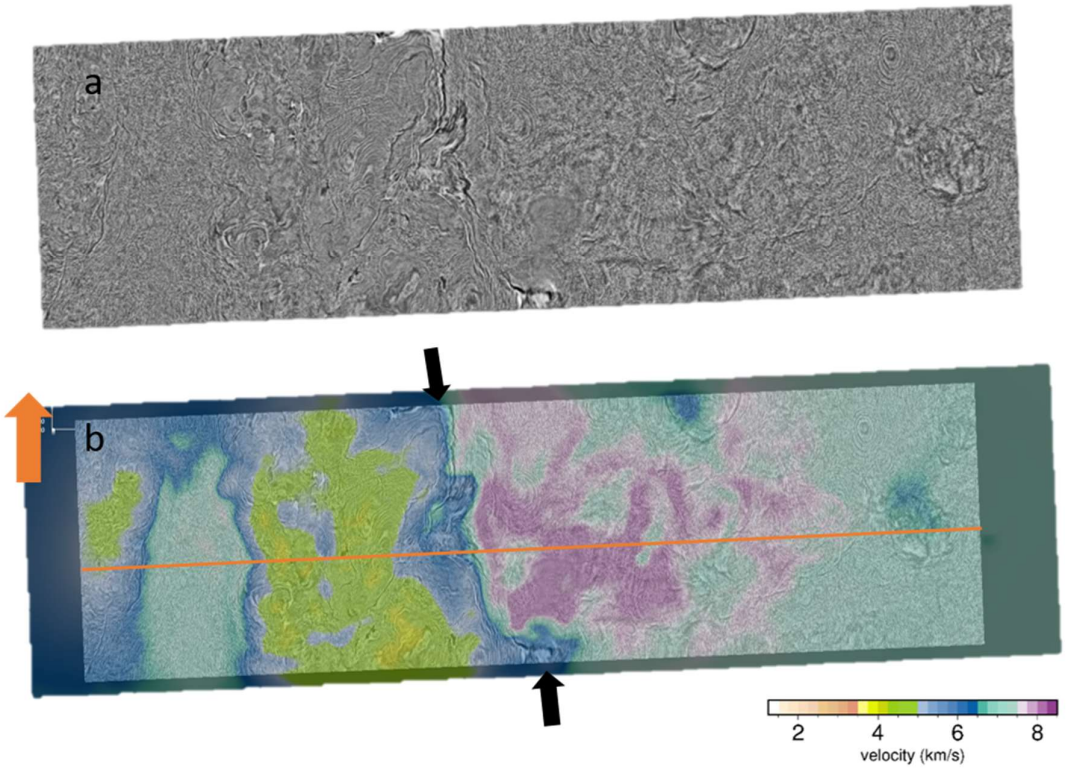

Figure 12 | Time slice extracted at 9.1 s two-way traveltime a) time slice from the multichannel volume b) 3DB FWI model overlaid on the time slice. Black arrows point to the boundary between the crust and upper mantle. North is shown by orange arrow. Line 2 is shown in orange.

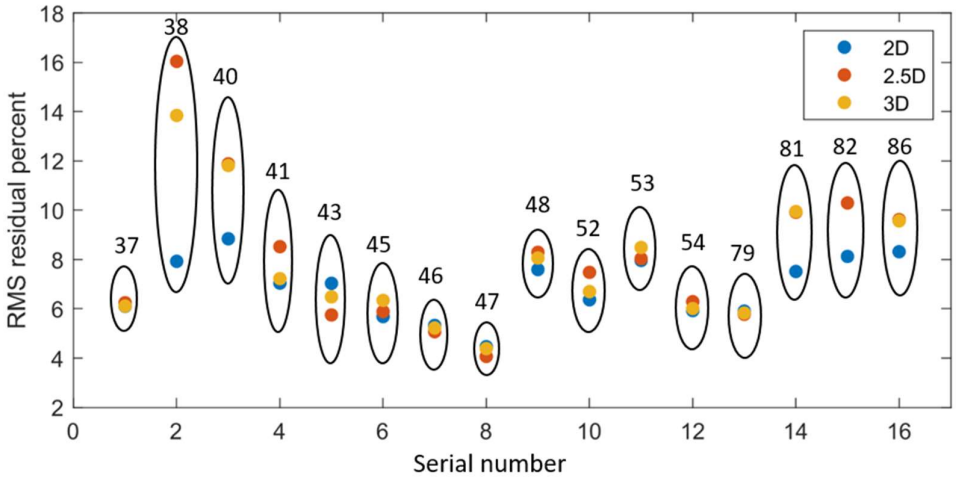

Figure 13 | RMS percent of the residuals for 2D, 2.5D and 3D (2DB, 3DA and 3DB) for each OBS along line 2 within oval shaped circles in black with OBS numbers on their top.

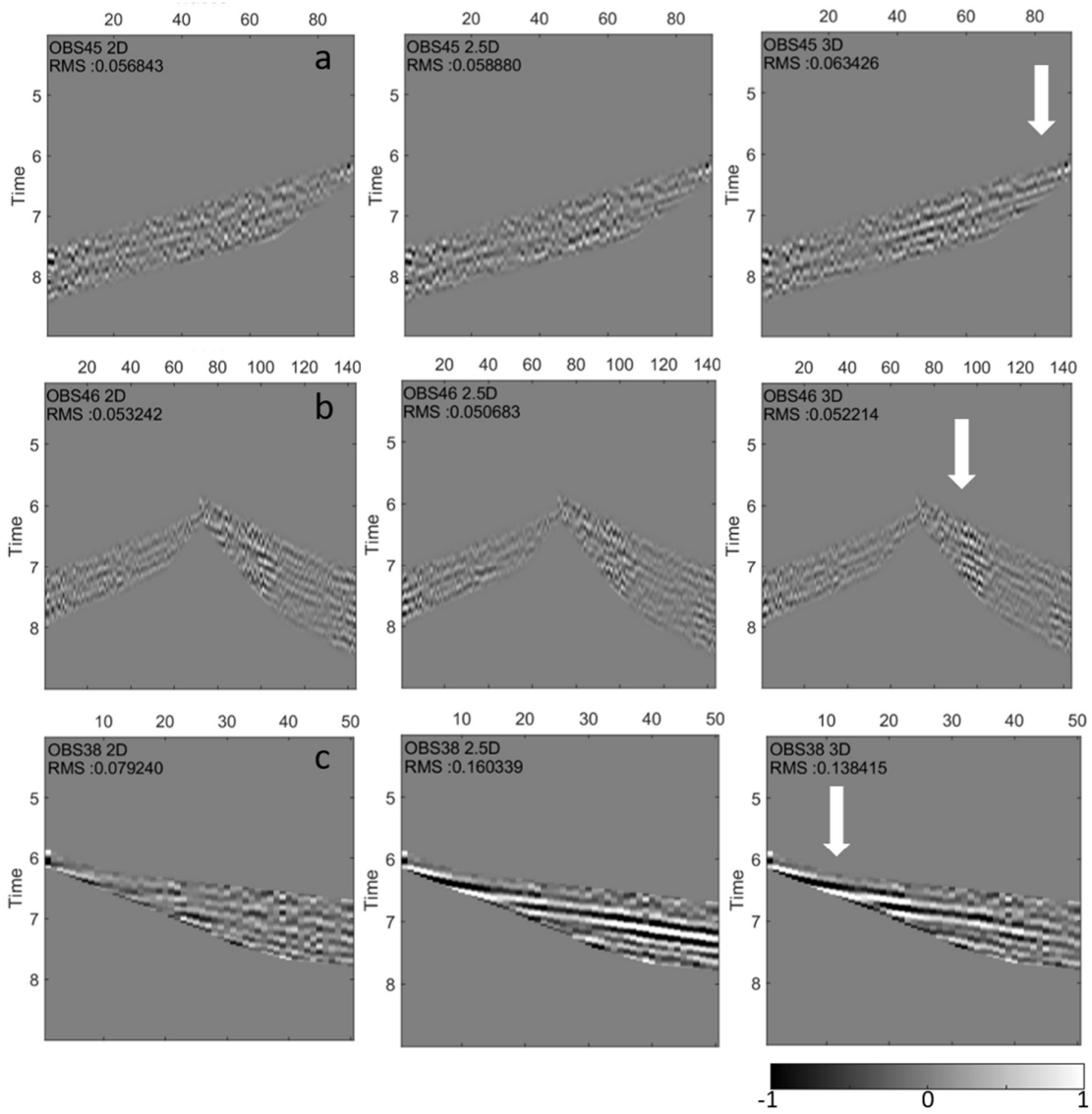

Figure 14 | Data residual plots of the normalised observed and synthetic datasets for the 2DB, 3DA and 3DB models for OBS 45 (a), 46 (b) and 38 (c) along the closest shooting profile to the instruments. Each panel shows the OBS number, number of dimensions of the inversion, and RMS value of the residuals. The white arrows indicate the nearer offsets arrivals.

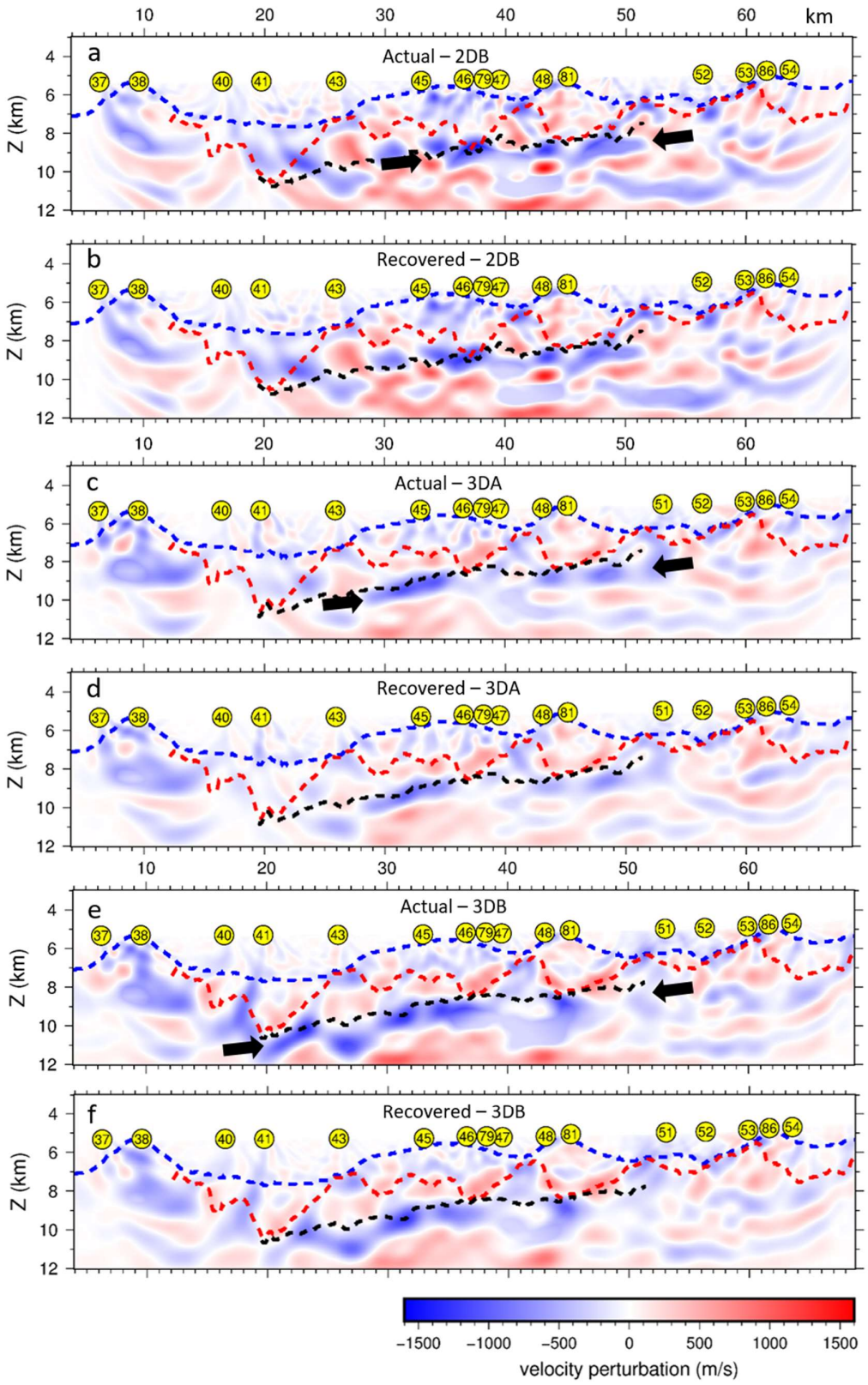

Figure 15 | a) Difference plot of the 2DB model and the starting model. b) Difference between the recovered anomaly model and the starting model. c) Difference plot of the 3DA model and the starting

model. d) Difference between the recovered 3DA anomaly model and the starting model. e) Difference plot of the 3DB model and the starting model. f) Difference between the recovered 3DB anomaly model and the starting model. The black arrows indicate a blue anomaly that progressively extends below the S from 2D to 3D. The interpretations are same as in figure 8 for respective profiles.

Appendix A:

Table 1:

OBS number	Number of shots
56	3917
57	6445
59	6314
61	8193
62	8899
63	3961
64	9835
66	6921
67	5751
68	4899
70	12693
71	6651
37	6930
38	375
40	247
41	6120
43	6129
45	11618
46	12381
47	12659
48	7797
51	8818
52	6924
53	5675
54	4032
19	4237
20	2745
21	10230
25	18881
26	16603
27	4823
29	15640
30	18379
31	6461
34	8566
35	14345
79	265
81	298
82	285
86	201

Appendix B: Observed and predicted data using the final 3D model (3DB) plotted in sets of 10 traces from all OBSs, alternating to show the match between the arrivals along the closest profile to the OBSs. The data shown are band-pass filtered (observed data) and trace-by-trace normalised.

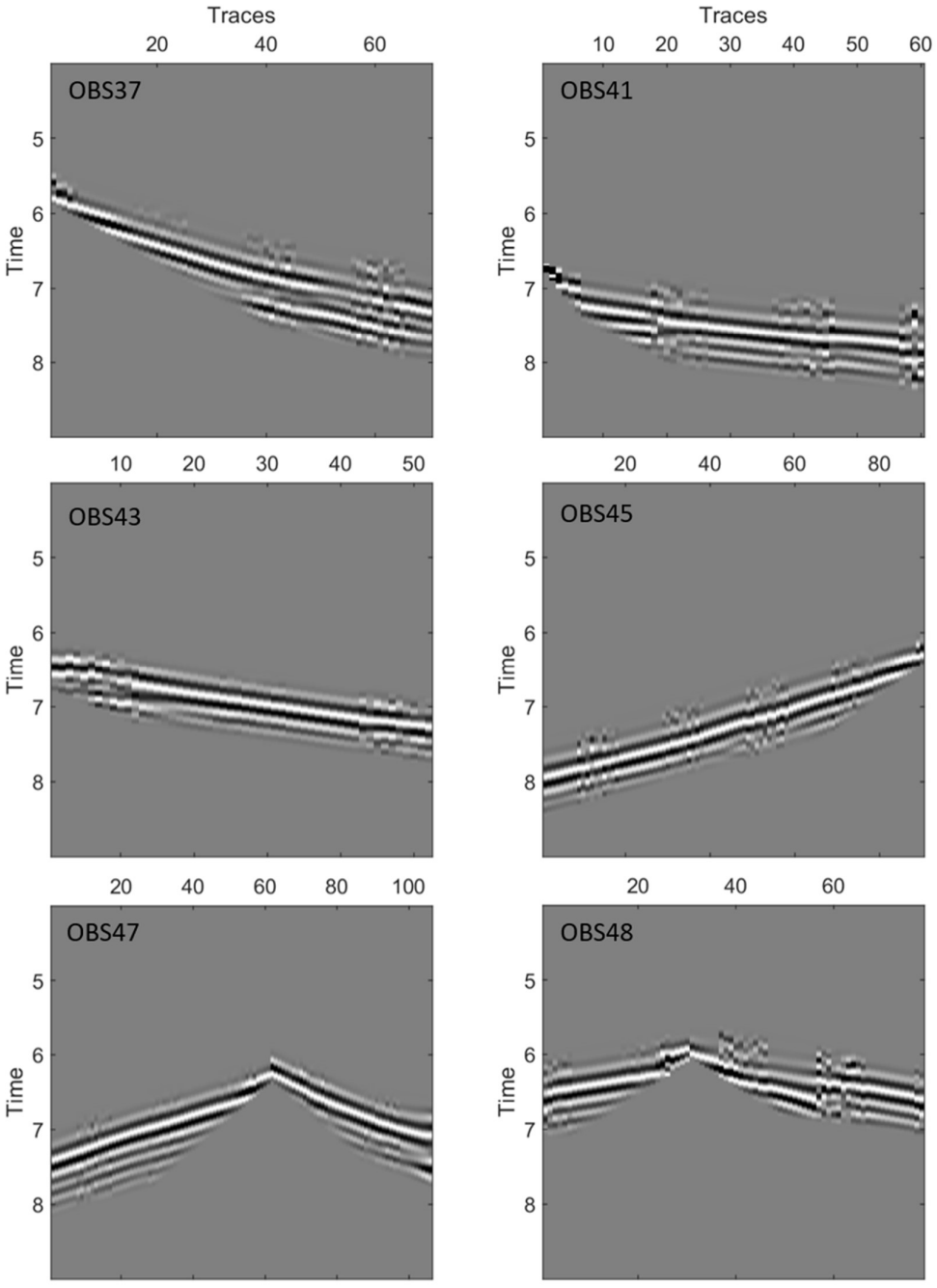

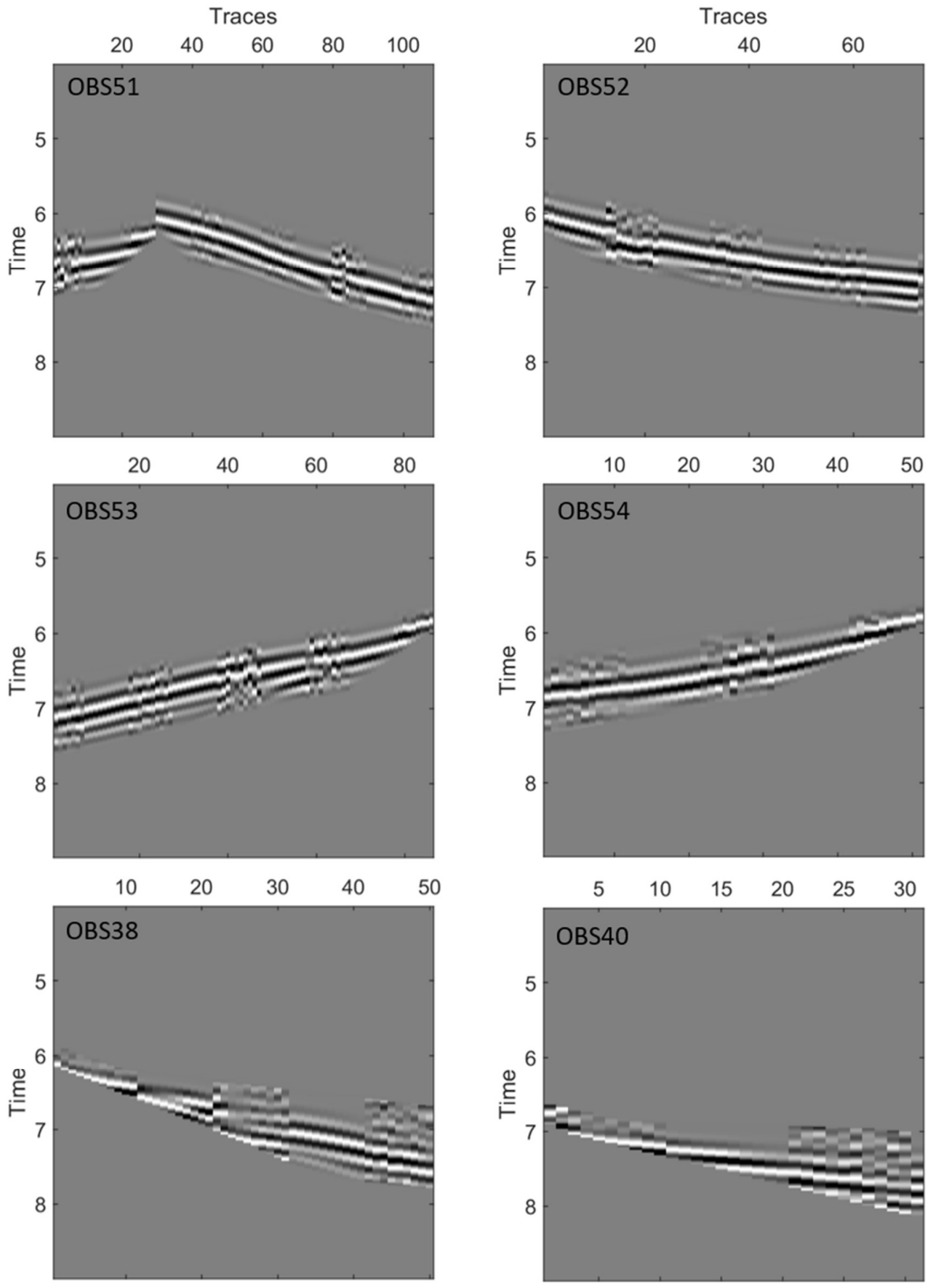

1213
1214

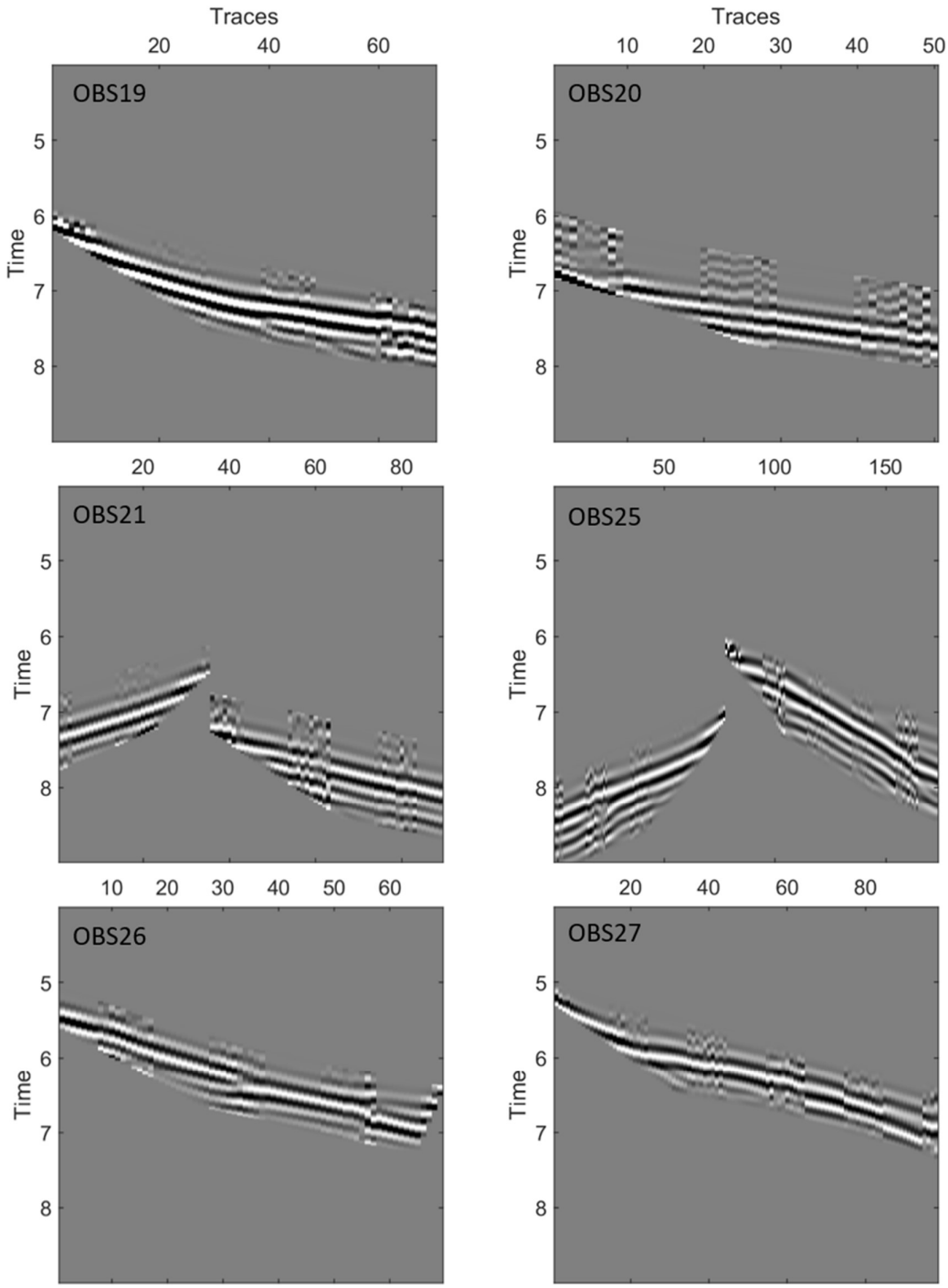

1215
1216
1217
1218

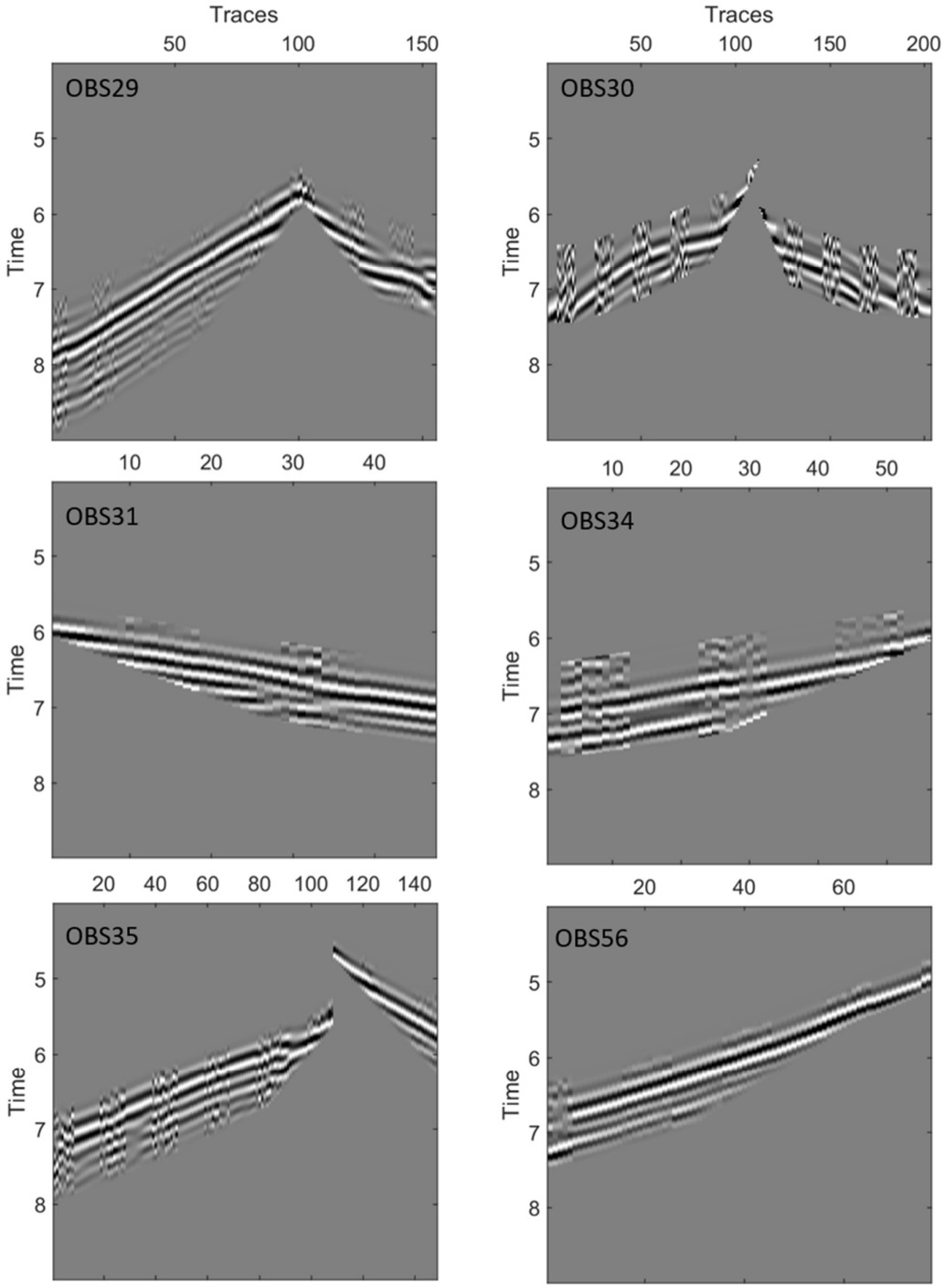
Traces
OBS29
Time
OBS30
OBS31
OBS34
OBS35
OBS56

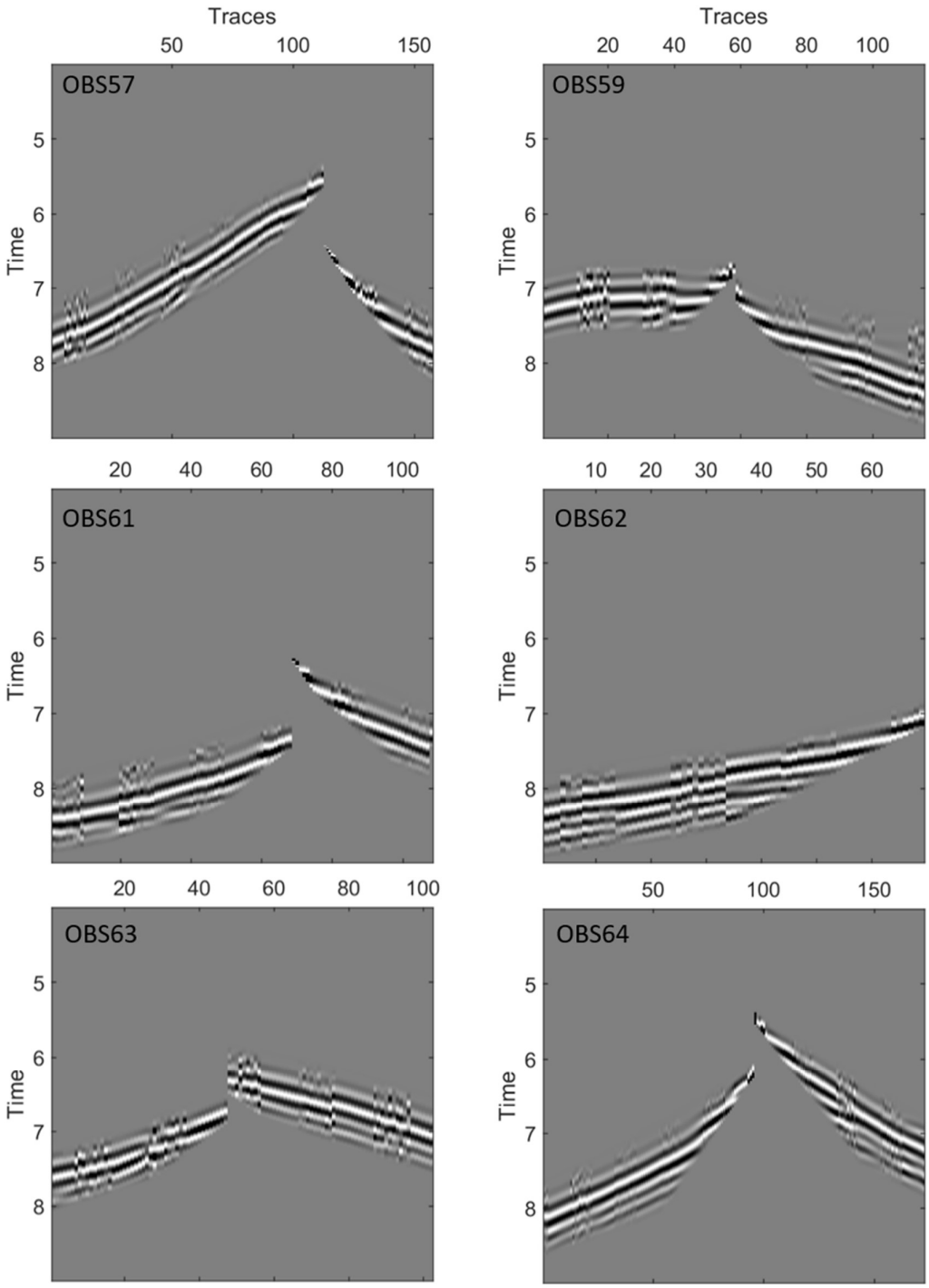

1228
1229
1230
1231
1232
1233
1234
1235

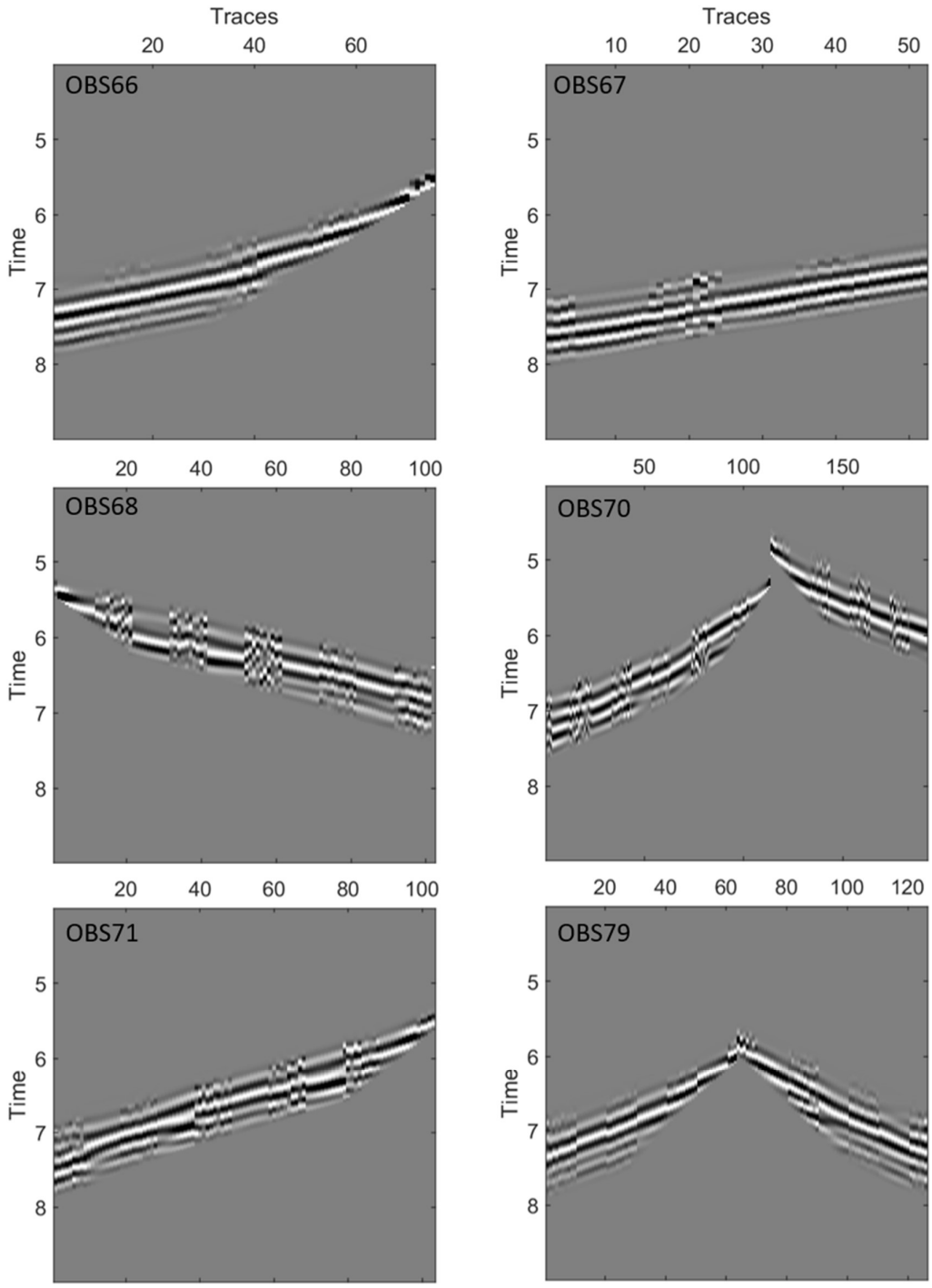

1236
1237
1238

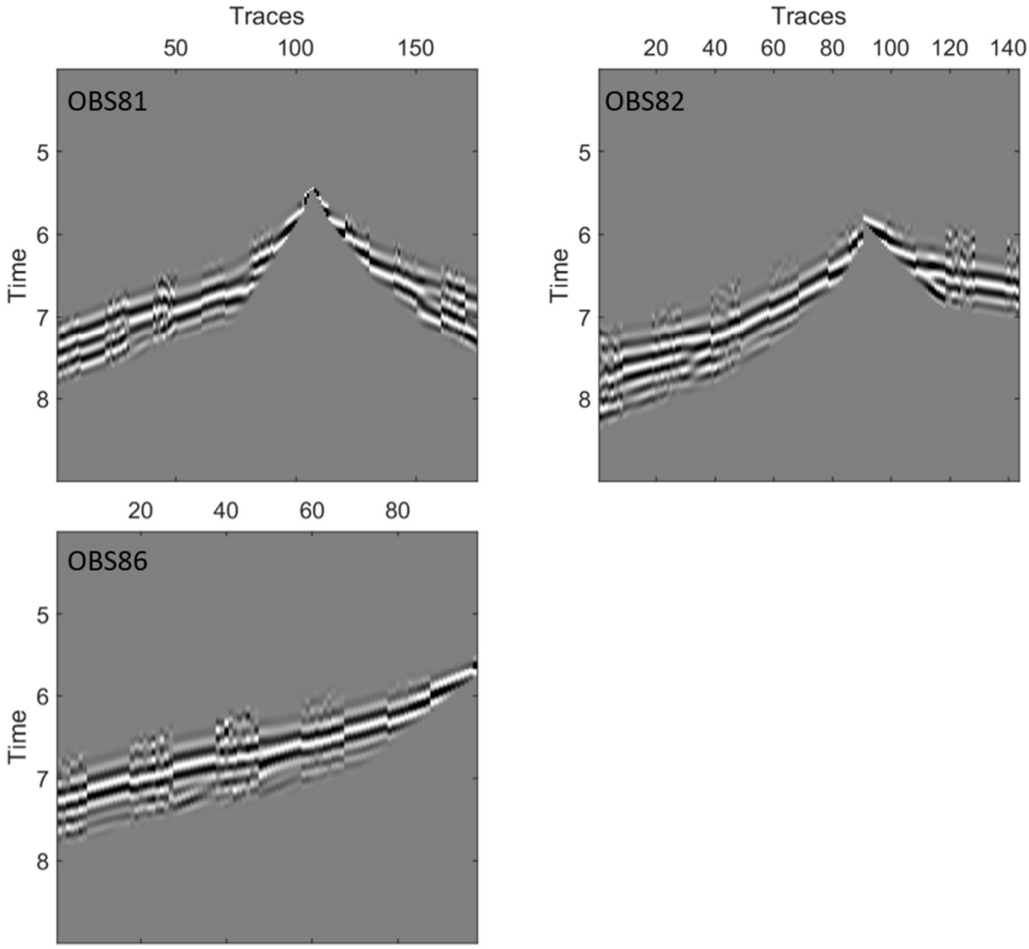
Traces
50
100
150
OBS81
Time
5
6
7
8
Traces
20
40
60
80
100
120
140
OBS82
Time
5
6
7
8
20
40
60
80
OBS86
Time
5
6
7
8

Appendix C: Data residual plots of the normalised observed and synthetic datasets for the 2D, 2.5D and 3D models for OBSs of line 2 along the closest shooting profile to the instruments. Each panel indicates the OBS number and the RMS value of the residuals.

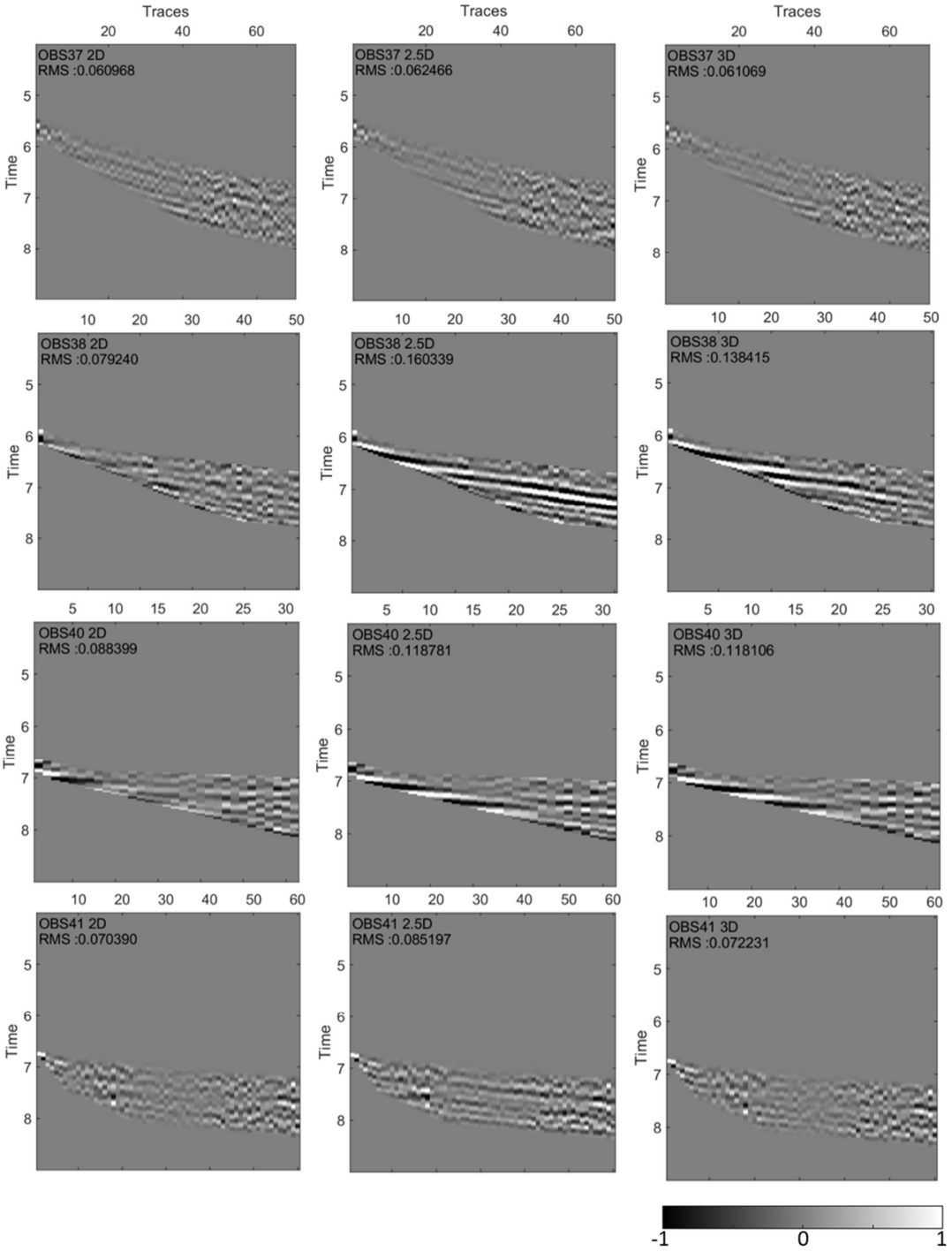

1265

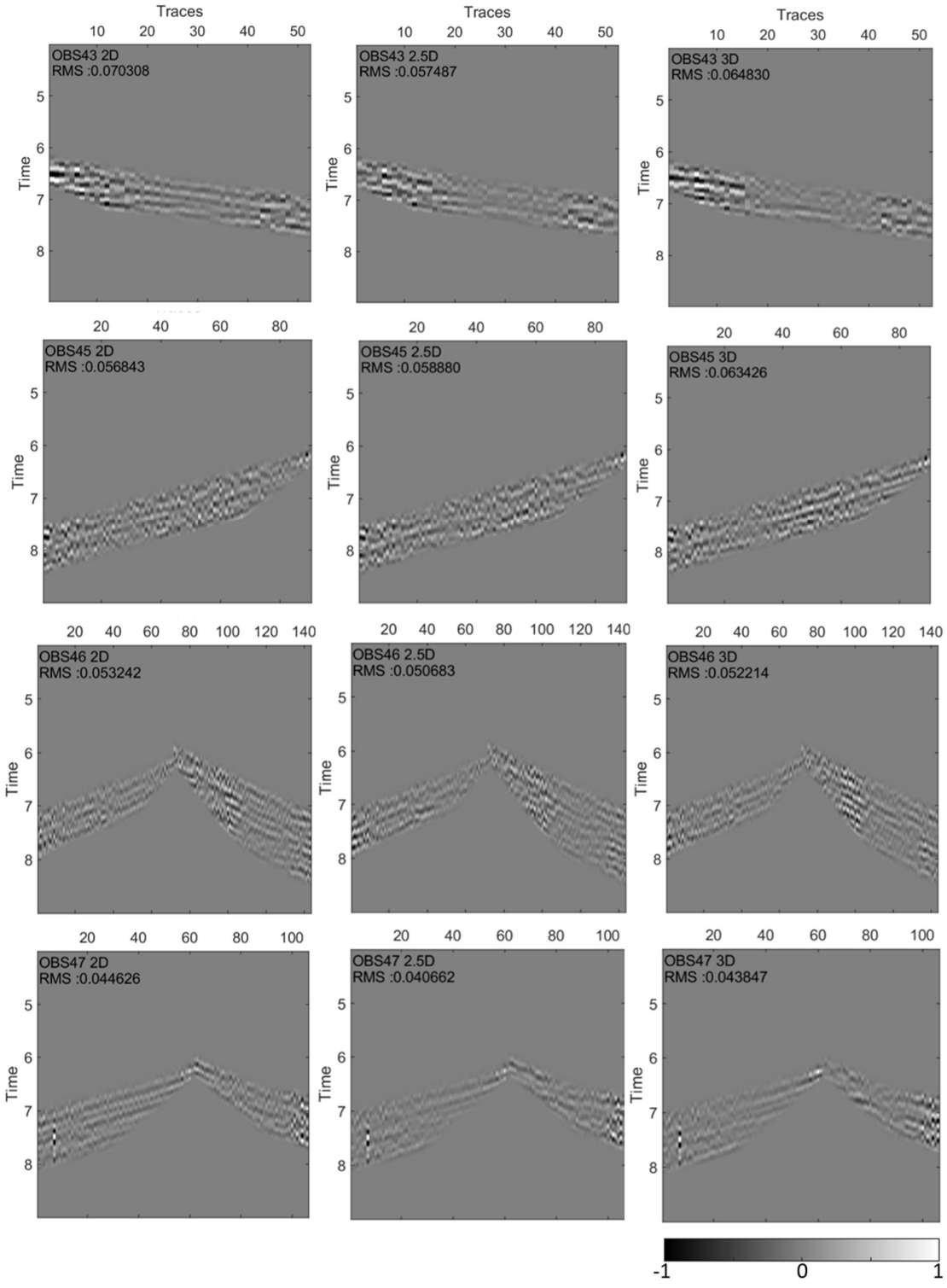

1266

1267

1268

1269

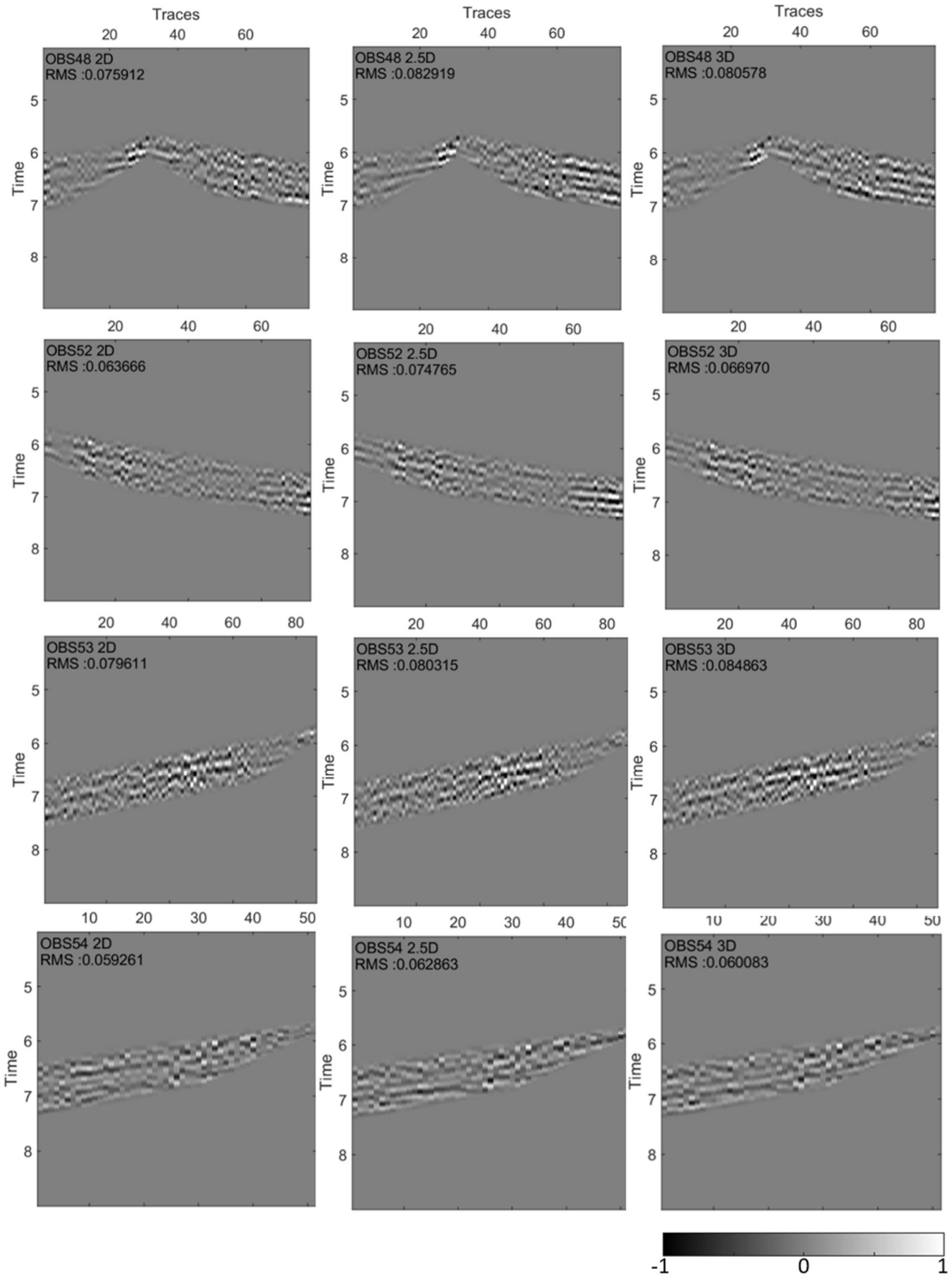

1270

1271

1272

1273

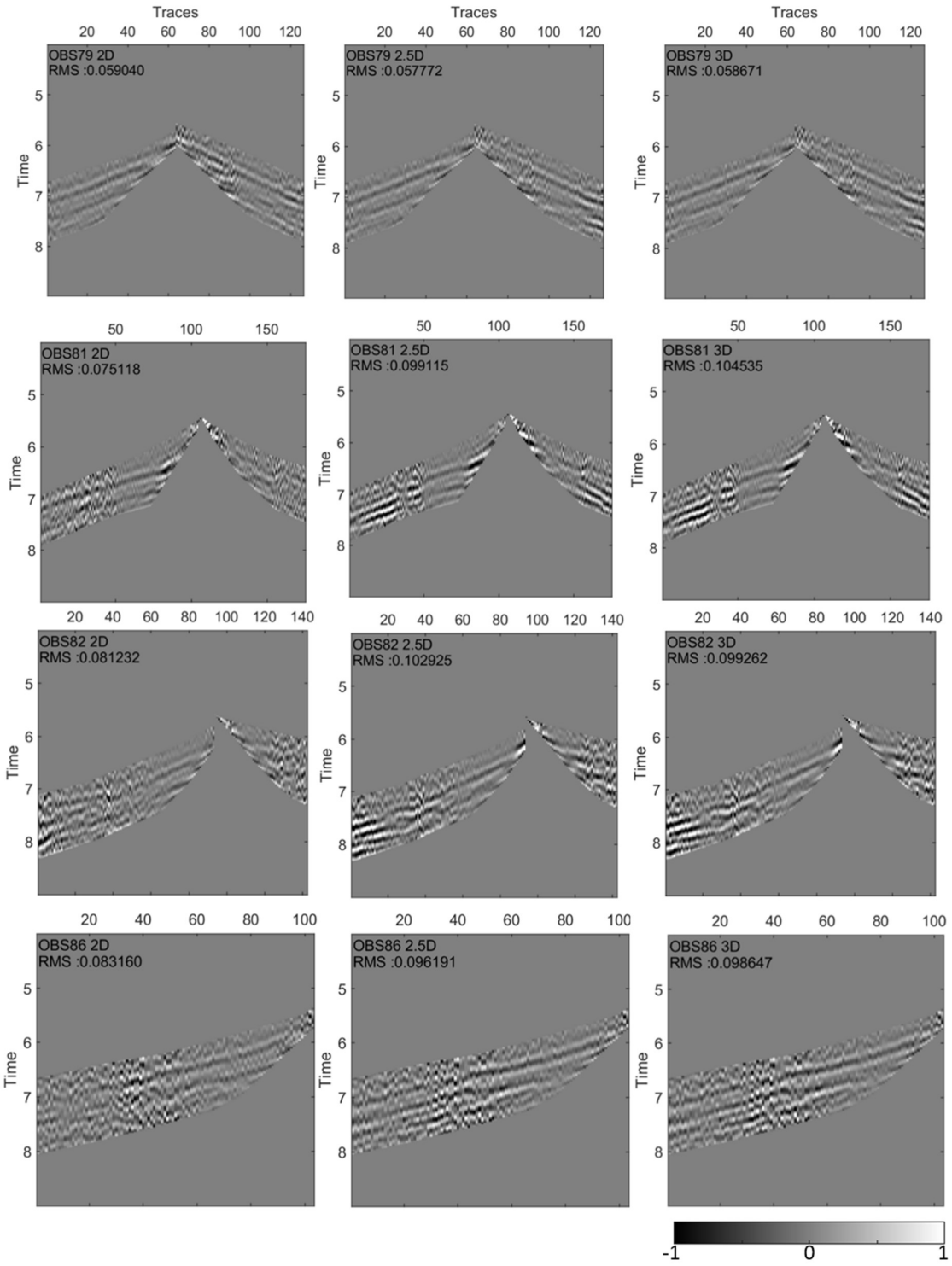

1274

1275

1276

1277